Temporal variations of the segmentation of slow to intermediate spreading mid-ocean ridges. 2. A three-dimensional model in terms of lithosphere accretion and convection within the partially molten mantle beneath the ridge axis

Michel Rabinowicz, Anne Briais

JOURNAL OF GEOPHYSICAL RESEARCH, VOL. 107, NO. B6, 2110, 10.1029/2001JB000343, 2002

Temporal variations of the segmentation of slow to intermediate spreading mid-ocean ridges
2. A three-dimensional model in terms of lithosphere accretion and convection within the partially molten mantle beneath the ridge axis

Michel Rabinowicz
Laboratoire de Dynamique Terrestre et Planétaire, UMR 5562, Observatoire Midi-Pyrénées, Toulouse, France

Anne Briais
Laboratoire d'Etudes en Géophysique et Océanographie Spatiales, CNRS, UMR 5566, Observatoire Midi-Pyrénées, Toulouse, France

Received 30 May 2000; revised 15 June 2001; accepted 13 September 2001; published 12 June 2002.

[1] We present three-dimensional numerical models of convection within the partially molten mantle beneath the ridge axis. The modeling takes into account the cavity flow driven by plate spreading, the diffuse upwelling due to plate accretion, and the shearing movement generated by large-scale mantle flow. The ridge axis is free to move in the spreading direction to adjust to the maxima of tension at the lithosphere-mantle interface induced by the convective circulation. The melt distribution in the mantle and the crustal production at the ridge axis are estimated using the formalism of *McKenzie and Bickle* [1988]. During the experiments the record of the ridge axis positions and crustal production is used to compute synthetic maps of the isochrons and oceanic crustal thickness. Close to the ridge, the ascending convective flow consists of 80- to 100-km-long hot sheets oriented either roughly parallel or orthogonal to spreading. Most ridge segments fit with the top of hot upwelling sheets, while transient transform faults coincide with the top of cold downwelling flows. The crustal maps display lineations subparallel or slightly oblique to spreading, a few tens of million years long, and separated by $\sim$60–50 km, resulting from the lithospheric record of the excess crust produced at the junction of hot sheets. When a junction of two hot sheets migrates outside the ridge axial plane, the crustal thickness maximum splits into two maxima along axis, and the induced lineation in the crustal map splits into two branches. The merging of lineations occurs when the ridge plane traps the junction of hot sheets. When the large-scale mantle circulation moves parallel to the ridge crest, it slowly pushs the spreading-parallel convective sheets. The resulting lineations form V shapes pointing in the same direction as the large-scale flow. When the large-scale flow parallels spreading, it slowly pushes the ridge-parallel hot sheets in the upflow direction. Thus the ridge segments attached to these hot sheets also migrate in the upflow direction. After several tens of million years the cavity flow driven by the spreading closes most of the transform segments and collects most of the ridge segments to form large continuous lines quasi-orthogonal to spreading. Using the relationships between crustal lineations and convective flow in the models, we interpret the lineations described in the satellite-derived gravity maps on the flanks of the Atlantic, Indian, and South Pacific plate boundaries analyzed in the companion paper by *Briais and Rabinowicz* [2002]. *INDEX TERMS:* 3010 Marine Geology and Geophysics: Gravity; 3035 Marine Geology and Geophysics: Midocean ridge processes; 8120 Tectonophysics: Dynamics of lithosphere and mantle—general; 8121 Tectonophysics: Dynamics, convection currents and mantle plumes; *KEYWORDS:* Mid-ocean ridge, mantle convection, ridge segmentation, gravity lineations, oceanic crust, mantle melting

0148-0227/02/2001JB000343$09.00

1. Introduction

[2] In the companion paper, *Briais and Rabinowicz* [2002] present a synoptic analysis of the 50-km wavelength gravity lineations on the flanks of slow to intermediate spreading mid-ocean ridges, inferred to result from the time record of either excess axial crustal production over mantle upwellings (“magmatic lineations”) or crustal thinning at axial offsets (“geometric lineations”) [*Briais and Rabinowicz*, 2002]. The distribution and orientation of the geometric and magmatic lineations, and their 20–100 km characteristic spacing, support the hypothesis that magmatic lineations are not generated by passive mantle upwelling but by a transient small-scale mantle flow in the partially molten mantle layer, with a wavelength of ~50 km, partially independent of the plate dynamics, which evolves during periods of time of several tens of million years. Moreover, the correlation between the regional obliquity of the lineations with respect to spreading, the spreading asymmetry, and the position of the closest hot or cold mantle plume suggests an interaction between small-scale and large-scale mantle flow beneath the ridge. In the present paper, we develop a model of mantle flow in the partially molten mantle layer beneath the ridge axis which accounts for most of the first-order observations.

[3] Small-scale mantle flow in the partially molten mantle may be driven by density changes due to mantle depletion, melt retention, and thermal convection [*Sotin and Parmentier*, 1989]. Melt retention results from the transient, intergranular flow transporting the melt produced in mantle upwellings. Mantle depletion results from the irreversible Fe/Mg decrease in the residual peridotite during melt extraction. Convection is generated by mantle cooling at the lithosphere-asthenosphere interface. The buoyancy forces resulting from melt retention, depletion, or convection have similar amplitudes. A peridotite with 5% melt presents a 1% density contrast with an unmelted peridotite. A depleted peridotite affected by 15% of melt extraction has a density contrast of ~1% with a lherzolite. In a mantle convective system, a 1% density contrast is due to the temperature difference between hot and cold flows. However, models suggest that these three processes have distinct effects on the dynamics of mid-ocean ridge accretion. Depletion slows down the subridge mantle upwellings and favors stratification of the depleted layer. Melt retention and mantle convection drive mantle upwellings which are three-dimensional under specific conditions. The buoyancy field due to interstitial melt splits the mantle flow within the ridge plane into discrete, focused, three-dimensional upwellings, only when the rate of retention is relatively high (several percent) [*Jha et al.*, 1994; *Choblet and Parmentier*, 2001]. Small-scale convection beneath the ridge axis induces the development of both three-dimensional upwellings and downwellings, not only within the ridge plane but within the entire partially molten domain, provided the Rayleigh number of the small-scale convection is several times 1708 the critical value for the onset of free convection [*Rabinowicz et al.*, 1993]. These flows do not develop instantaneously but develop after the several million year period necessary to generate the convective boundary layers. Moreover, the convective circulation shows a transient evolution lasting more than 100 Myr before a quasi-steady state is reached [*Rabinowicz et al.*, 1993; *Rouzo et al.*, 1995]. Models including both melt retention and mantle convection show first the quasi-instantaneous development of focused upwellings triggered by the buoyancy forces due to melt retention and, several million years later, the generation of convective rolls with axes parallel to spreading, located several hundred kilometers from the ridge plane [*Barnouin-Jha et al.*, 1997]. The latter study did not investigate the long-term evolution of the flow resulting from the time-dependent reorganization and magnification of the convective flow.

[4] Owing to the long timescale at which geometric and magmatic lineations evolve, the physical process responsible for them can only be related to small-scale convection. Consequently, in the present paper, we calculate the temporal evolution of the segmentation and crustal production induced by a three-dimensional (3-D), transient, small-scale convection flow that develops due to thermal buoyancy in the partially molten mantle layer beneath ridges.

[5] A major difference between recent models of subridge mantle flow concerns the choice of appropriate rules to account for melt migration processes. *Jha et al.* [1994], *Barnouin-Jha et al.* [1997], and *Choblet and Parmentier* [2001] estimate the interstitial melt concentration using a steady Darcy law. *Jha et al.* [1994] suggested that the rate of melt retention strongly decreases with the radius of the grains composing the solid fraction of the mush. According to Jha et al. a rate of retention of ~0.3% and 5% is expected when the radius of the solid grain is 3 mm and 0.3 mm, respectively. Surface seismic wave observations lead to estimates of the melt concentration of 1–5%, depending on the topology of the melt channels [*MELT Seismic Team*, 1998; *Webb and Forsyth*, 1998]. These estimates represent a mean melt concentration at a kilometer scale. Data recovered in ophiolites show that the concentration of interstitial melt in the mantle mush varies from much less than 1% in places, and up to 100% in local melt impregnations [*Ceuleneer and Rabinowicz*, 1992; *Ceuleneer et al.*, 1996]. These observations suggest that the melt transport operates as pulses discontinuous in space and time. This conclusion is consistent with recent models of the generation of transient melt waves in the mantle mush [*Scott and Stevenson*, 1986; *Spiegelman*, 1993; *Wiggins and Spiegelman*, 1995; *Connolly and Podladchikov*, 1998; *Ghods and Harkani-Hamed*, 2000]. Data indicate that melt migrates at rates of the order of 60 m yr^{-1}, while thermal convective upwellings have upward velocities of the order of 60 mm yr^{-1} [*Spiegelman and Elliot*, 1993; *Jull and McKenzie*, 1996]. Thus our model assumes that the processes of melt migration and mantle convection act at timescales that are so different they cannot be taken into account jointly in a numerical model. Compaction models suggest that after the waves propagate, the interstitial melt concentration is buffered at a critical value $m_c \approx 6\%$ [*Khodakovskii et al.* 1995, 1998; *Rabinowicz et al.*, 2001]. Beyond this threshold, the mantle rheology is soft because of the migration of dislocations in the interstitial magma films [*Hirth and Kohlstedt*, 1995]. These results show that it is only the melt concentration left after the propagation of the waves that contributes to the buoyancy field driving the plastic flow inside the mantle mush. According to this model the *S* waves velocity anomaly below ridges can thus likely be ascribed to m_c. Consequently, we propose to relate the melt retention in the mantle to m_c. This is an alternative to the approximation of steady Darcy

flow suggested by *Jha et al.* [1994] to estimate the concentration of interstitial melt produced during mantle upwelling.

[6] Along ascending currents of the convective flows the melt concentration remains equal to m_c. Within the top convective boundary layer and within dipping flows the melt recrystallization and flow reduce the interstitial melt concentration below m_c [*Scott*, 1992; *Turcotte and Phipps Morgan*, 1992; *Braun et al.*, 2000; *Rabinowicz et al.*, 2001]. Thus the buoyancy field due to the melt concentration drives the mantle either upward or downward in places where convection acts in the same way. We assume here a perfect proportionality between the buoyancy fields due to partial melting and temperature. This simplification contrasts with that made by *Barnouin-Jha et al.* [1997], who computed the melt retention and temperature fields separately. Our simplification is motivated by the numerical difficulty to monitor the melt concentration evolution during several convective cycles (see section 2).

[7] A second important simplification restricts the convection model to the partially molten mantle layer. This approximation follows from the vertical stratification of the mantle viscosity. In fact, the development of convective upwellings or diapirs in the mantle mush requires an effective viscosity of $\sim 10^{18}$ Pa s [*Rabinowicz et al.*, 1984; *Whitehead et al.*, 1984; *Buck and Su*, 1989; *Sparks et al.*, 1993]. Glacial rebound data and geoid-to-topography ratio over swells suggest that the 200-km-deep low seismic velocity channel beneath oceanic plates has a viscosity of $\sim 10^{20}$ Pa s [*Cathles*, 1975; *Robinson and Parsons*, 1988; *Monnereau et al.*, 1993]. Finally, the agreement between large-scale components of the Earth's geoid anomaly and topography fields with those derived from whole mantle convection suggests a viscosity jump of an order of magnitude at the spinel-postspinel transition zone [*Ricard and Wuming*, 1991]. Thus the vertical profile of mantle viscosity beneath the ridge axis probably displays several steps, increasing from $\sim 10^{18}$ Pa s in the mantle mush to $\sim 10^{22}$ Pa s in the lower mantle. Presently, there is no systematic study of the flow structure of a whole mantle convective cell crossing, from top to bottom, four layers of increasing and constant viscosity. Such a model is impossible to implement because it requires an explicit resolution of the 3-D convective equations with a huge number of grid points. Simulations with only two viscosity layers show that the large-scale, high-viscosity convective flow consists in hot and narrow ascending plumes with polyhedral downwelling sheets [*Rabinowicz et al.*, 1990]. When the Rayleigh number of the large-scale convection reaches a threshold value of ~ 3.105, small-scale convection develops inside the top, low-viscosity layer at some distance from the hot plume [*Dubuffet et al.*, 2000]. Thereafter, the radially divergent flow driven by these plumes shears the small-scale convection in a manner reminiscent of the one observed when shear is imposed at the top of a convective layer [*Richter and Parsons*, 1975]. *Barnouin-Jha et al.* [1997] studied the superposition of the large-scale flow driven by plate spreading and the convection confined within the upper low-viscosity mantle layer. Their results show that a segmented, small-scale flow develops inside the ridge plane only when the spreading velocity is slow or intermediate. This modeling provides an explanation for the absence of 50–100 km gravity lineations along the Pacific ridge flanks and their observation over most of the Atlantic and Indian Ridges [*Sparks et al.*, 1993; *Parmentier and Phipps Morgan*, 1990; *Phipps Morgan and Parmentier*, 1995; *Barnouin-Jha et al.*, 1997]. These studies suggest ways to analyze the interactions of small-scale convection with the large-scale flow through a model of convection restricted to the mantle mush.

[8] Finally, the constant viscosity used in our model to study convection in the partially molten layer is justified by the buffering of the melt concentration at the $m_c \approx 6\%$ threshold value. Moreover, structural data in the harzburgite and dunite units of the transition zone of most ophiolite massifs, and in particular those of Oman, indicate that the mantle remains very soft even when the melt concentration reaches a fraction of 1%, thus much lower than the threshold value $m_c \approx 6\%$ [*Ceuleneer and Rabinowicz*, 1992]. This puzzling and fundamental observation follows from the local interstitial melt migration and redistribution during plastic deformation. In a strained rock, melt accumulates in planes subparallel to the direction of maximum shear. The bulk intergranular melt concentration may be as low as a fraction of 1% while the effective viscosity of the mantle mush remains low. The equations describing this process have been solved by *Stevenson* [1989], and the rheological law of the mush integrating the melt redistribution was studied in the laboratory by *Daines and Kohlstedt* [1997]. Models and data suggest that the effective viscosity law describing plastic flow of the mush is stress- and melt-dependent and that the relationship between effective viscosity, stress, and melt concentration is strongly nonlinear. The modeling of convection with a non-Newtonian rheology shows that the temperature and flow field obtained are similar to those with a constant viscosity, except close to the corner of the cells, where the streamlines rotate with a very acute angle [*Parmentier et al.*, 1976; *Christensen and Harder*, 1991]. In summary, we see that the processes controlling the rheology of the partially molten mantle tend to homogenize its viscosity field, implying that the use of a constant viscosity inside the mantle mush is a plausible choice.

[9] Adopting these simplifications, we use 3-D numerical models to study small-scale convection forced by plate spreading, plate accretion, and the horizontal, large-scale diverging flow driven by hot or cold mantle plumes. Using the successive positions of the ridge axis and the corresponding crustal production at the ridge axis during the 90-Myr duration of our 3-D numerical experiments, we compute synthetic isochron and crustal maps of the seafloor. Our goal is to understand the relationships between ridge segmentation, plate spreading, plate accretion, large-scale mantle flow, small-scale convection, and the geometric and magmatic lineations generated at the ridge crest. The equations, mathematical tools, and equations of states used in our modeling are given in section 2 and in Appendix A. The models are shown in section 3. Their essential features are discussed in section 4. The implications of our results for the segmentation of mid-ocean ridges are discussed in section 5.

2. A model of Convection and Melt Extraction in the Mantle Mush

2.1. Flow Model

[10] The model simulates the cavity flow generated in the mantle mush by two diverging plates above a large-scale

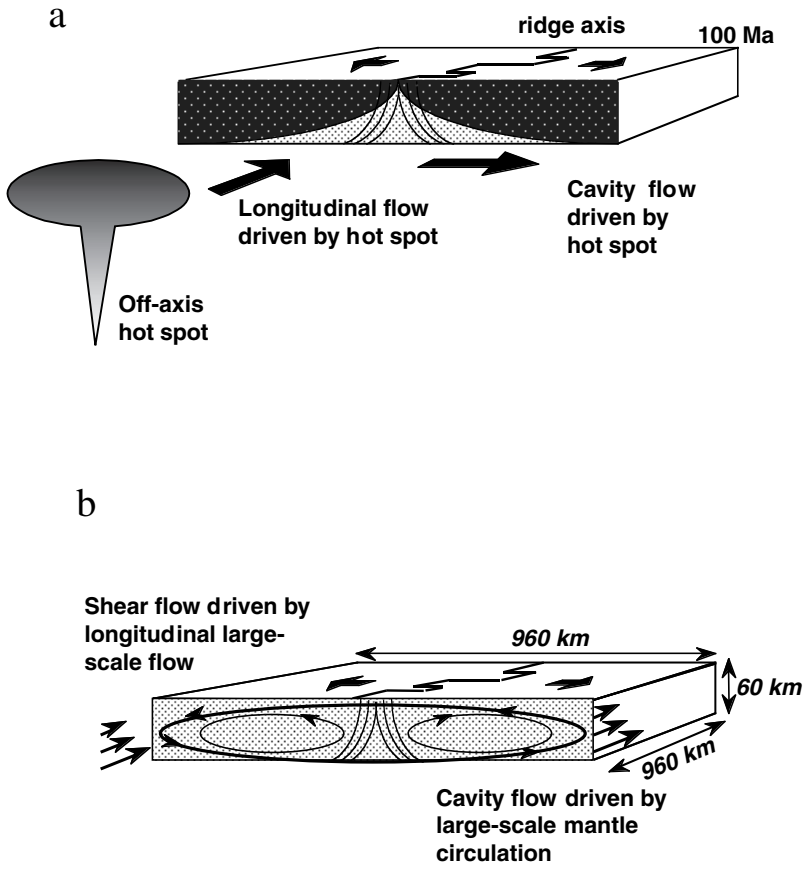

Figure 1. (a) Sketch of mantle flow in the partially molten mantle layer during oceanic lithosphere accretion and spreading. Curving streamlines of the cavity flow driven by plate spreading are also sketched. The lithosphere is drawn as solid, and the mush is a dotted pattern. (b) Illustration of the boundary conditions and geometry of the mantle mush adopted in our modeling. We used a set of 256 × 256 × 21 grid points to run cases with a Rayleigh number Ra = 30,000 and 256 × 256 × 42 grid points to run Ra = 90,000 cases.

mantle convective current (Figure 1). The half-spreading velocity V_{accr} ranges between 8 and 34 mm yr^{-1}. The thickening of the lithosphere with age generates a diffuse flow across the entire mushy layer, sucking undepleted mantle through the bottom of the mush. To simplify the computation, we neglect the decrease in thickness of the low-viscosity layer due to lithospheric accretion. Thus this interface is set horizontal along the z = 0 plane and at a pressure of 0.38 GPa. Here z is the vertical coordinate, taken positive downward, and 0.38 GPa corresponds to the mantle pressure 15 km below sea level. The bottom of the partially molten layer is planar and lies at a 75 km depth, close to the garnet stability field. It results that the mush layer is a parallelepiped with a thickness D = 60 km. It is 16D long in the direction of spreading (here parallel to the x axis) and 16D large along the ridge direction (here the y axis). The layer has a constant viscosity. Because of the strong viscosity contrast between the mantle mush and the underlying mantle the recirculation flow driven by plate spreading and the convective instabilities generated in the mush are only marginally advected inside the underlying mantle, except at the top of downwelling sheets of the whole mantle convective structures [*Rabinowicz et al.*, 1993; *Sparks et al.*, 1993; *Dubuffet et al.*, 2000]. Accordingly, we assume here that the recirculation flow and the convective flow do not cross the bottom interface of the computing box. This last assumption implies that we are modeling the convection inside the mantle mush at some distance from any hot or cold spot of the whole mantle convection. The recirculation flow is shaped by the thinning of the mushy layer due to plate thickening in the direction of spreading. In our model the partially molten layer has a large horizontal extent. *Barnouin-Jha et al.* [1997] showed that the geometry of the mushy zone only plays a minor role on the convection planform which develops just beneath the ridge axis. In section 4.2 we show that it also likely has a moderate influence on the ridge axis segmentation and drift.

[11] The numerical experiments start with an unsegmented ridge. Thereafter, it is free to migrate, in the spreading direction, according to the nearest tensile stress maxima induced by the convective flow in the overriding elastic lithosphere. This method of estimation of the position of the ridge crest is described by *Rouzo et al.* [1995]. It provides a fairly realistic simulation of geometric segmentation of slow to intermediate spreading mid-ocean ridges. Details of the calculation of the elastic stress field in the lithosphere are given in Appendix A. In the model we use

the classic relationship between the plate thickness d_{lith} and its age [*Parsons and Sclater*, 1977]:

$$d_{\text{lith}}(t) = C\sqrt{t}. \tag{1}$$

We adjust the dimensional constant C to place the brittle-ductile interface at 60 km for 100 Ma. It results that the flow accreted along this mantle-mush interface has a vertical velocity verifying:

$$r(x,y) = -\frac{C}{2\sqrt{\Delta(x,y)/V_{\text{accr}}}}, \tag{2}$$

where $\Delta(x,y)$ designates the distance from the top grid (x,y) to the ridge axis. At each time step we update the vertical velocity at the top of the computing box using the new distances $\Delta(x,y)$ to the ridge axis. This mass flow is provided by a diffuse mantle upwelling through the bottom of the mush layer. Because of the strong viscosity contrast between the mush and the underlying mantle this flow generates a negligible strain at the bottom of the mush. Consequently, the vertical velocity along this interface is essentially constant. Actually, we adjust it so that the bottom upwelling flow matches the one accreted at the lithosphere-mush interface. When V_{accr} = 17 mm yr^{-1}, it is equal to 1.1 mm yr^{-1}. In the spreading direction x the vertical sides of the computing box are planes of symmetry of the velocity field. Because of the strong viscosity step at the bottom of the mush we assume that the cavity flow driven by the top plate shearing has a zero velocity at the bottom of the mush. To construct models in which flow is free to move in the direction orthogonal to spreading, we constrain it to be periodic in the y direction in multiples of $16D$ = 960 km.

[12] Finally, we simulate the presence of a large-scale flow driven by hot spots by adding a shear flow, generated by a constant velocity $\mathbf{V}_{\text{bot}}$ applied to the bottom interface of the computing box, to the flow field generated by convection, top spreading, and top accretion. Let us write

$$\mathbf{V}_{\text{bot}} = (U_{\text{bot}},\ V_{\text{bot}}), \tag{3}$$

where U_{bot} and V_{bot} designate the bottom speeds in the spreading direction x and ridge direction y, respectively. Because of the boundary condition adopted along the vertical walls of the computing box this shear generates a shear flow inside the box $U_{\text{ridge}}(z) = U_{\text{bot}}z/D$ in the along-ridge direction y and a cavity flow $V_{\text{cav}}(x, z)$ in the spreading direction x (Figure 1). The cavity flow $V_{\text{cav}}(x, z)$ and the shear flow $U_{\text{ridge}}(z)$ are found to play a major role in the evolution of the convective circulation and the segmentation and drift of the ridge axis. We discuss the validity of these conditions in terms of coupling between small- and large-scale mantle convection in section 4.4.

2.2. Melt Extraction Model

[13] To evaluate the rate of melting within the mush, we use the approximations made by *McKenzie and Bickle* [1988]. Inside the hot upwelling flow the temperature T exceeds the mantle solidus T_s which can be approximated in the 0.25- to 2.5-GPa lithostatic pressure P interval by

$$T_S(P) = 1100^{\circ}\text{C} + 136P. \tag{4}$$

The fraction by weight of melt produced in a mantle peridotite, $\chi(T, P)$, can be fit by

$$\chi(T,P) = 0.5 + \theta + \left(\theta^2 - 0.25\right)(0.4256 + 0.2988\theta), \tag{5}$$

where θ is the following nondimensional temperature function:

$$\theta = \frac{T - T_s(P)}{T_l(P) - T_s(P)}. \tag{6}$$

In (6) the $T_l(P)$ function which designates the liquidus of the mantle is approximated by

$$T_l(p) = 1736.2^{\circ}\text{C} + 4.343P. \tag{7}$$

2.3. Convective Model

[14] The equations of conservation of mass, momentum and energy are

$$\nabla \cdot \mathbf{V} = 0, \tag{8}$$

$$-\nabla_p + \eta\nabla^2\mathbf{V} + \rho_m\mathbf{g}\alpha T' = 0, \tag{9}$$

$$\frac{\partial T'}{\partial t} + \mathbf{V}\nabla \cdot T' = \kappa\nabla^2 T', \tag{10}$$

where $\mathbf{V}$ is the velocity vector with components (u, v, w) in the Cartesian coordinate, P is the dynamic pressure, η is the viscosity, ρ_m is the mantle density, α is the coefficient of thermal expansion, and κ is the coefficient of thermal diffusivity. Also, $\mathbf{g}$ and g designate the gravity vector and the gravity acceleration, respectively. The values of the model parameters are given in Table 1. In these equations, T' represents the potential temperature, i.e., the temperature corrected from the cooling due to decompression and melting. The convective layer being thin, the temperature decrease due to decompression depends linearly on depth (the adiabatic temperature gradient is $\sim$0.3–0.4°C km^{-1}) and the heat sources produced by shear are negligible [*Jarvis and McKenzie*, 1980]. Also, completely melting the peridotite decreases its temperature by $\sim$300°C. In our models the melting within the upwelling convective flow ranges between 6% and 32%, with a mean of 16% (see section 4.3). As a result, the melting cools the ascending flow by $\sim$60°C. The local rate of cooling due to melting is proportional to $d\chi/dt$ (equation (5)). Explicit introduction of this term in the resolution of the equation of temperature (equation (10)) is difficult because it leads to a nonlinear coupling of the melting and convection processes [*Scott and Stevenson*, 1989]. To simplify the computations, the cooling term due to melting is not included in the temperature equation. Instead, we assume that it is constant along the entire upwelling flow. This implies that as a first-order approximation, the cooling process due to melting linearly

Table 1. Physical Parameters of the Models

Parameter	Value
Acceleration of gravity g	10 m s^{-2}
Mush thickness D	60 km
Mush density ρ_m	3.3×10^3 kg m^{-3}
Thermal expansion α	3×10^{-5} K^{-1}
Temperature at the	
Lithosphere-mush interface	1090°C
Bottom of the mush	1470°C
Adiabatic cooling	0.3 K km^{-1}
Cooling due to melting	60°C
Specific heat	1200 J K^{-1} kg^{-1}
Thermal diffusivity κ	0.75×10^{-6} m^2 s^{-1}
Viscosity μ	
When Ra = 30,000	2.3×10^{18} Pa s
When Ra = 90,000	0.7×10^{18} Pa s
Elastic thickness h	2000 m
Young's modulus E	1.5×10^{11} Pa
Poisson's ratio ν	0.28

depends on the rate of decompression, like adiabatic cooling. Accordingly, we assume a linear relation between the temperature T and the potential temperature T':

$$T(x,y,z,t) = T'(x,y,z,t) + \Delta T(z/D), \tag{11}$$

where $\Delta T \approx 20°C + 60°C = 80°C$ is the bottom-to-top cooling due to adiabatic decompression and melting. In the model we set a temperature T_{sup} of 1090°C along the top boundary, and a temperature T_{inf} of 1470°C along the lower one [*Langmuir et al.*, 1992]. At the lower interface the lithostatic pressure is 2.5 GPa. The equation of state leads to a melt fraction χ just exceeding the concentration threshold $m_c \approx 6\%$ (Figures 2–6). The temperature of 1090°C likely represents the brittle-ductile transition temperature of the mantle rocks. In agreement with the boundary condition for the flow equation set along the vertical faces of the computing box, we assume (1) a symmetrical temperature field along the vertical sides of the box orthogonal to the spreading direction (x direction) and (2) a periodic temperature field in the along-ridge direction (y direction) with a wavelength of 16D.

[15] In the flow equation (9), there is no buoyancy term for the melt concentration. The latter decreases within the top convective boundary layer and inside the dipping flows, an effect which increases the magnitude of the buoyancy term due to the temperature field. As indicated in section 1, the buoyancy field due to the melt and the one due to the temperature field are roughly proportional. In fact, the contribution of the interstitial melt buoyancy on convection is roughly equivalent to doubling the thermal expansion coefficient α. The linear relationship chosen for the latent heat rate of cooling/or freezing with depth assumes that the warming up of downwellings due to the freezing of melt equals the cooling of upwellings due to melting. Hence the melt extracted from the mantle along the ridge creates a thermal imbalance which increases the temperature contrast between upwellings and downwellings [*Ito et al.*, 1999]. The convective pattern being 3-D, downwellings mix the return flows of the upwellings located beneath the ridge with those of the upwellings located away from it. The melt extraction is specific to the ridge axis because it is triggered by the lithospheric stretching or the dynamical depression in the mantle due to plate spreading [*Sotin and Parmentier*, 1989; *Barnouin-Jha et al.*, 1997]. Thus mantle downwellings mix depleted and undepleted rocks. In our models (see section 4.2) the mean melting rate in mantle upwellings is 16%, and two thirds of it is extracted from the mantle along the ridge axis. Following these remarks, at most 50% of the downwelling flow consists of mantle which has lost 10% of melt. Accordingly, the latent heat due to the production of crust likely minors the temperature of downwellings by ~20°C. It increases the buoyancy of thermal convection by 8%: a small value compared to the factor of 2 ascribed to the buoyancy of interstitial melt. Note that the precise computation of the buoyancy and heat loss due to interstitial melt depends on the monitoring of the melt migration and crystallization processes, which are extremely difficult to implement in the present regional 3-D modeling of the long-term, transient evolution of small-scale mantle convection [*Smaltzl et al.*, 1995]. Moreover, the assumed proportionality between the temperature and interstitial melt fields allows decoupling of the calculation of the convective flow from that of the melt fraction χ, which is critically dependent on the rough petrological data fitting realized by *McKenzie and Bickle* [1988].

2.4. Evaluation of the Crustal Thickness and Initialization of the Model

[16] Since the melt concentration in excess of m_c is transported by porosity waves to the lithosphere-mush interface, the melt flow along the lithosphere-mush interface satisfies [*Watson and McKenzie*, 1991]

$$q(x,y) = \int_0^D \rho_m \frac{d\chi}{dt}(x,y,z)dz = \int_0^D \rho_m \left(\frac{d\chi}{dT}\chi\nabla^2 T' - w\rho_m g \frac{d\chi}{dz} \right) dz. \tag{12}$$

This integral is evaluated in the melting zones (domains of positive values for the melting rate $d\chi/dt$) and in the zones where the melt concentration exceeds $m_c \approx 6\%$. Notice that $\chi(x,y,D) \approx m_c$.

[17] The ridge axis can be considered as a door open to the melt flow pooling along the lithosphere-mush interface. The width of the axial region in the spreading direction is limited by the thickening of the lithosphere. Let us assume that its width on both sides of the ridge crest is a, then the thickness of the crust at the ridge axis dc (y) is

$$d_c(y) = \frac{1}{2\rho_c V_{accr}} \int_{-a+\delta(y)}^{+a+\delta(y)} q(x,y)dx, \tag{13}$$

where ρ_c designates the crust density, and $x = \delta(y)$ the function relating the along-strike to spreading-parallel positions of the ridge axis. In the present modeling, $a \approx$ 9 km, a value consistent with the horizontal extent of subridge magma bodies and the thickness of the convective boundary layer of our model.

[18] After each time step the new ridge position is used to calculate the new forced flows, which are finally added to the convective flow to update the thermal field. As usual, computations are run using nondimensional variables. The

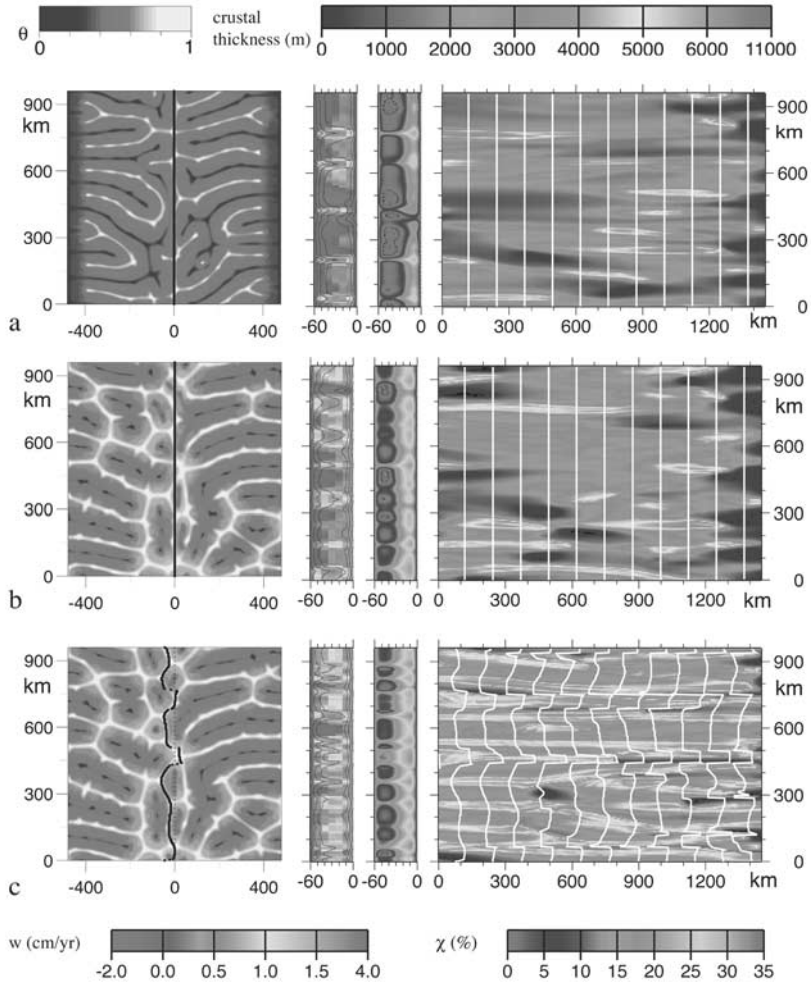

Figure 2. Comparison of three distinct, 90-Myr-long experiments with a Ra = 30,000, a half-spreading velocity V_{accr} = 17 mm yr^{-1} and a bottom shear $\mathbf{V}_{bot}$ = 0. In the first two experiments the ridge axis position is fixed (Figures 2a and 2b), while in the last one it migrates as explained in the text and Appendix A (Figure 2c). In the first model the upwelling driven by plate accretion is not added to the flow field (Figure 2a). The maps at the left represent the final snapshot of the middepth horizontal nondimensional thermal field, bright colors designate hot fluids with close to 1, and dark ones designate cold fluids with close to 0. The initial position of the axis is marked by a north-south dotted line and the final position by solid lines. (right) Isochron and crustal thickness on the eastern flank of the oceanic plate. The isochrons at 8 Myr-interval are drawn in plain white lines, and the crustal thickness is in color. Scales of color for the crustal maps are drawn at the top. The middle left box shows vertical velocity w in the ridge plane and temperature at the end of each experiment. Isotherms are drawn in plain black lines. The middle right box displays melt fraction by weigh along the ridge plane. Color scales for w and for are shown at the bottom. See color version of this figure at back of this issue.

single nondimensional parameter measuring the free convection intensity is the Rayleigh number Ra:

$$Ra = \frac{\rho_m g \alpha (T_{sub} - T_{inf} - \Delta T) D^3}{\kappa \eta}. \quad (14)$$

In fact, among the parameters in (14), the mush viscosity is the only one whose amplitude is known only to within 1 order of magnitude. Thus choosing a Rayleigh number determines mush viscosity. In the present study, we use Rayleigh numbers of 30,000 and 90,000. These values are consistent with a viscosity range from 2.25×10^{18} Pa s to 0.75×10^{18} Pa s.

[19] The flow field is written in terms of poloidal and toroidal scalar fields. Then the equation of motion leads to a biharmonic equation and a harmonic equation for the poloidal and toroidal parts, respectively. These equations are solved using a Fourier horizontal decomposition and a vertical finite difference one. This method is detailed by *Rabinowicz et al.* [1993]. The temperature equation is solved using a finite difference method known to give good results in 3-D modeling of mantle convection [*Douglas and Rachford*, 1956; *Blankenbach et al.*, 1989]. Convection

with motionless boundaries and a Rayleigh number ranging between 24,000 and 100,000 has a bimodal flow structure: that is, it consists of the superposition of two sets of orthogonal rolls. However, when we initiate our experiments with a random thermal field, we never obtain a perfect set of orthogonal rolls in a reasonable period of time. The time needed to reach the 3-D, asymptotic, steady state regime is proportional to several times the conductive time D^2/κ, i.e., several times 160 Myr [*Whitehead and Parsons*, 1978]. Hence we choose to start our numerical experiments with the 16 Ma snapshot of the thermal field of a convective case run with zero top and bottom shearing velocities ($V_{accr} = \mathbf{V}_{bot} = 0$), and initiated with the temperature field:

$$T(x,y,z) = T_{top} + (T_{inf} - T_{top})\left[\frac{z}{D} + 0.05\sin\left(\pi\frac{z}{D}\right)\mathrm{ranf}(x,y)\right], \quad (15)$$

where ranf (x,y) designates a random function with a unit mean amplitude.

3. Experiment Results

[20] In order to get a progressive insight on the relationships between convection and magmatic or geometric ridge segmentation we present several experiments which differ by the Rayleigh number or by the flow conditions set along the top and bottom interfaces of the computing box.

3.1. Cases With a Small Rayleigh Number and No Bottom Shear

[21] Figure 2a displays a case with a Rayleigh number $Ra = 30{,}000$, a top half-spreading velocity $V_{accr} = 17$ mm yr^{-1} and a zero horizontal bottom velocity $\mathbf{V}_{bot} = 0$. In this experiment the ridge axis is maintained straight and parallel to the y direction and we do not take into account the diffuse flow resulting from plate accretion. At the end of the 90 Ma experiment the convective flow consists in a set of intersecting rolls. Over 100 km from the ridge, the rolls whose axes are parallel to the ridge direction are quite damped, and those parallel to the spreading direction concentrate the essential part of the flow and temperature heterogeneity [*Richter and Parsons*, 1975]. In the following, we designate this last type of rolls as Richter's rolls. The spacing between the successive, parallel Richter's rolls is ~110–150 km. Close to the ridge, there is a continuous set of hot ascending sheets, subparallel to the ridge direction, which zigzag on both sides of the axial plane. In the vicinity of the ridge axis, curving streamlines of the cavity flow induced by the top spreading delineate a roof-shaped domain, where the mantle is fairly still (Figure 1). In fact, this quiescent domain favors the development of these ridge-parallel, hot upwelling sheets. Most of the Richter's rolls are connected to these sheets. Where they intersect, the flow is strong and hot, producing more crust than elsewhere along the axis (Figure 2a, right). Since the experiment begins with a convective flow which is not symmetrical with respect to the ridge plane, the Richter's rolls below the eastern and western spreading plates are not necessarily connected to the same ridge-subparallel ascending sheets. The temperature, velocity, and melt fraction along the ridge plane at the end of the experiment reveal that the flow ascends along most of this plane, except along two narrow zones, above which the crustal production is null (Figure 2a, middle). Note that the mean crustal thickness produced during the 90 Ma experiment is 2 km. Magmatic lineations with a maximal crustal thickness of 9 km are produced above the intersections of Richter's rolls and ridge-parallel hot sheets.

[22] The introduction of the diffuse flow resulting from plate accretion drives a uniform, vertical upwelling with a 1.1 mm yr^{-1} intensity across the bottom boundary of the computational box. Although this flow does not alter the convective pattern, it does increase the flow intensity in the ridge-parallel hot sheets (Figure 2b). Several ridge-parallel upwelling sheets develop even far away from the ridge axis. Because of the strengthening of the spreading orthogonal flow the amplitude of the magmatic lineations increases and the mean crustal production averaged over the 90 Ma experiment reaches 2.3 km.

[23] In the following experiment the ridge axis is iteratively adjusted to follow the local maximum of tension generated by the convective circulation (Figure 2c and 3). The experiment is initiated with a straight ridge. The other parameters are those of the last experiment (Figure 2b). The convective circulation evolves slowly: The flow and thermal state after 8 Ma consist of a set of intersecting rolls remaining very close to the one used to initiate the experiment (Figure 3a). The ascending sheets form a zigzagging network of planes with a horizontal length of ~70 km. Stronger upwellings at the intersection of ascending sheets form hot plumes. Many of these plumes result from the intersection of two rolls only. However, plumes in which three distinct rolls originate are common. This last feature also occurs during the initiation of analogue laboratory experiments with similar Rayleigh numbers as a result of the "pinching" of two parallel rolls into a single one [*Busse and Whitehead*, 1974]. As time goes on, top shearing movement progressively reorganizes the flow, decreasing the number of convective rolls. After 90 Ma (Figure 3f) the spacing between successive parallel Richter's rolls is 110–150 km. It exceeds the initial spacing of the bimodal set of rolls by a factor up to 2 (Figure 3a). We observe that the ridge segments migrate either eastward or westward to sit above the closest ridge-parallel ascending sheet. When the ridge axis meets the ascending flow of a ridge-parallel roll, large continuous ridge segments develop (Figure 3a). The same snapshot shows that ridge segments initially located above Richter's rolls tend to migrate far from their first position (Figures 3a and 3f). This leads to the initiation of U-shaped transform-ridge-transform systems ~100 km in offset. The progressive reorganization of the convective flow leads to the progressive collapse of some transform offsets. Nevertheless, we note that U-shaped systems located above Richter's rolls are particularly stable (Figure 3). Also, in this experiment, two long ridge segments having captured two different, ridge-parallel rolls remain separated by a 100-km offset transform fault during the whole experiment. At the end of the 90 Ma experiment the ridge line tends to become more continuous and the convective flow structure remains strikingly similar to that obtained when the position of the ridge axis is held fixed (compare Figures 2a, 2b, and 2c,). This similarity suggests that the local adjustment of the ridge position only weakly

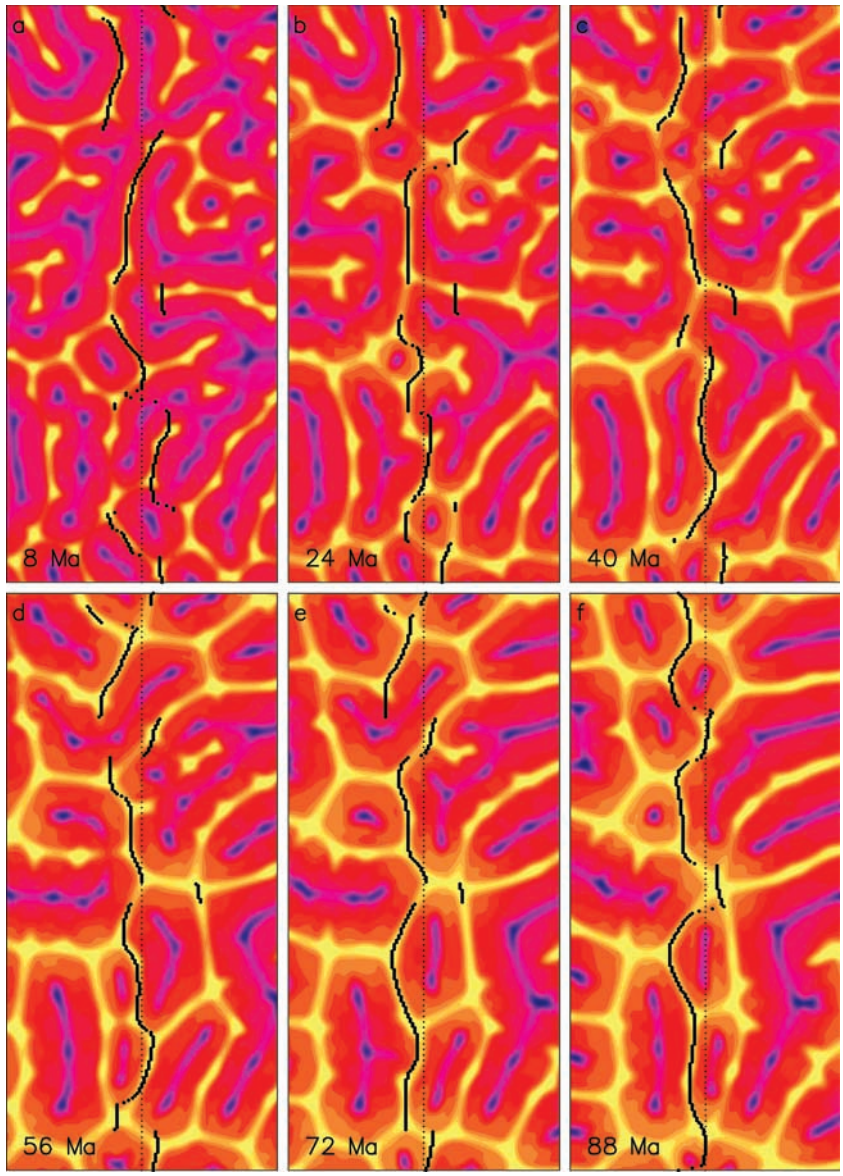

Figure 3. Evolution of the thermal field when Ra = 30,000, V_{accr} = 17 mm yr^{-1}, and $\mathbf{V}_{bot}$ = 0 (model also shown in Figure 2c), shown as snapshots of the middepth temperature in a window restricted to the central part of the computing box. Plotting conventions are as in Figure 2. See color version of this figure at back of this issue.

modifies the evolution of the convective flow. Figure 2c shows that the ridge segments coincide with the axis of the hot ascending sheets except at the vicinity of a transform offset where the local maximum of tension does not coincide with the roll axis. The convective snapshots show that the different ridge segments remain <100 km from the initial ridge line (Figure 3). The isochron and crustal map associated with this model (Figure 2c) show that the mean crustal production during the 90 Myr duration of the experiment is 3.5 km, ~50% thicker than in the experiments with a fixed ridge axis (Figures 2a and 2b). The increase in crustal thickness results from the fact that most of the ridge axial segments are now positioned above ridge-parallel hot sheets where melt production reaches its maximum. Figure 3 shows that only transient ridge discontinuities migrate along the ridge. Also, magmatic lineations tend to migrate along axis. Their drift results from the along-strike migration of the subridge hot plumes. They drift very slowly in comparison with the convective velocity: 200 km during ~50 Ma or 0.4 mm yr^{-1}.

[24] Strikingly, we observe several cases where two magmatic lineations merge (Figure 2c). It occurs when a pinching plume meets the ridge axis, for example, in the northern part of the plate boundary between 24 and 40 Ma (Figures 3b and 3c). The merging occurs when two ridge segments drifting above two distinct rolls ride over a point where the two rolls pinch into one. Conversely, the splitting of a magmatic lineation occurs where the ridge drifts above a spreading-parallel upwelling which then divides into two distinct sheets. The rate of melting, the temperature, and the velocity field on the ridge plane at the end of the experiment show that the mantle flow is ascending below the whole

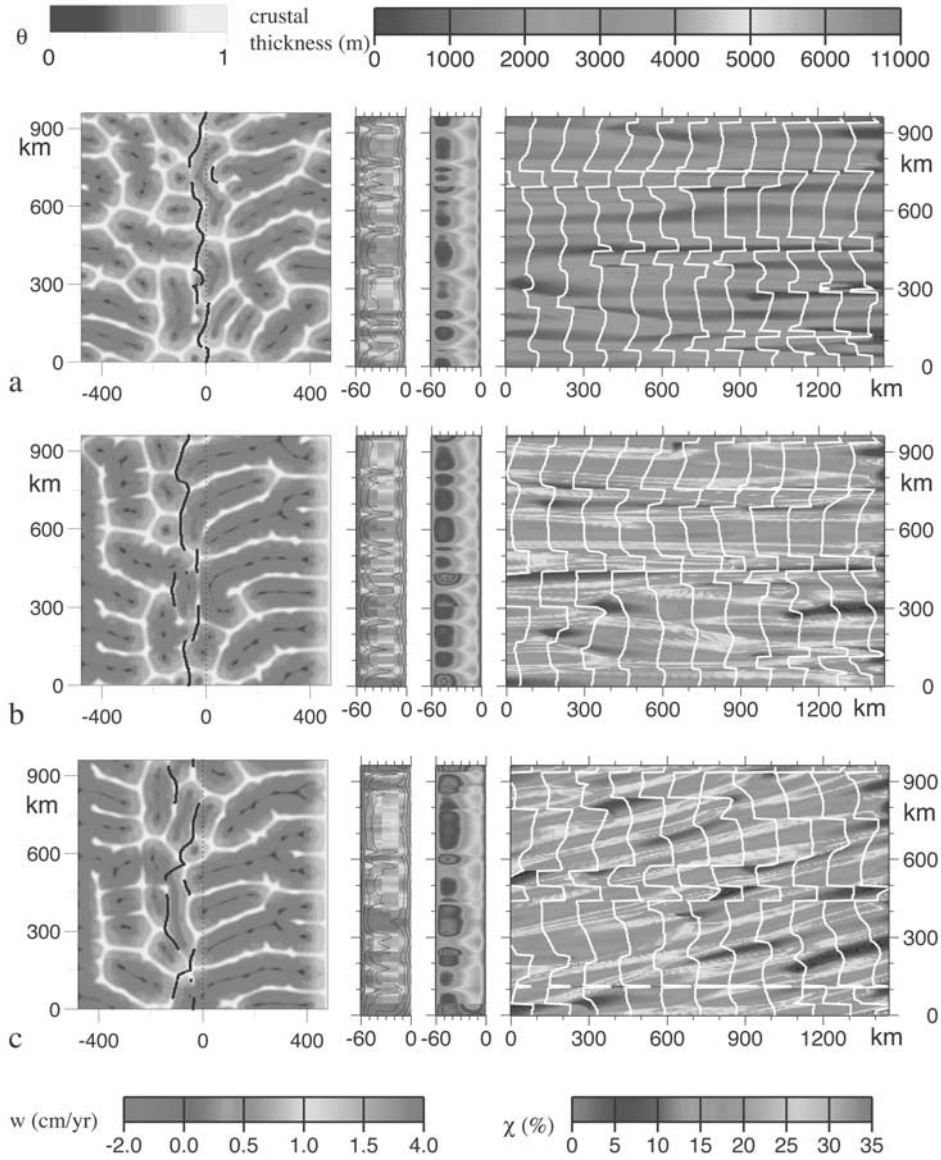

Figure 4. Three distinct experiments with Ra = 30,000. Plotting conventions as in Figure 2. The first experiment (Figure 4a) shows the effect of doubling the spreading velocity: V_{accr} = 34 mm yr^{-1} instead of 17 mm yr^{-1}. In the last two experiments (Figures 4b and 4c) we test the effect of a shear velocity at the bottom of the layer: $\mathbf{V}_{bot}$ = (8 mm yr^{-1}, 0 cm yr^{-1}) and $\mathbf{V}_{bot}$ = (8 mm yr^{-1}, 8 mm yr^{-1}), respectively. The experiments in Figures 4b and 4c last 90 Myr, while the one in Figure 4a lasts 45 Myr. Other parameter values are those of the model drawn in Figures 2c and 3. See color version of this figure at back of this issue.

ridge axis, except near a small domain in the central part of the plate boundary where the ridge axis sits above a dipping current (Figure 2c). In fact, Figure 3f shows that this ridge segment lies near a transient ridge discontinuity overriding an entire convective cell. As a result, the ridge crustal production is null at the intersection of the ridge axis and the dipping part of this convective cell.

[25] Figure 4a displays the situation when we double the half-spreading velocity V_{accr} to 34 mm yr^{-1}. Other parameter values are the same as those of the last experiment. The evolution of the convective circulation and the ridge adjustment observed at 45 Ma (Figure 4a) resembles the one recorded at 90 Ma when the spreading velocity is 17 mm yr^{-1} (Figure 2c). Since most of the flow along the ridge plane is advected upward by the free convection, the volume of melt produced along the ridge axis remains quite constant (Figure 4a), implying that the mean crustal thickness is now 1.8 km, i.e., just over half the mean crustal production recorded when V_{accr} = 17 mm yr^{-1}.

3.2. Experiments With a Small Rayleigh Number and a Bottom Shear

[26] In Figures 4b and 4c we display the evolution of the flow, the ridge position, and the crustal production when the bottom of the mush layer is sheared to the east with $\mathbf{V}_{bot}$ = (8 mm yr^{-1}, 0 mm yr^{-1}) and to the southeast with

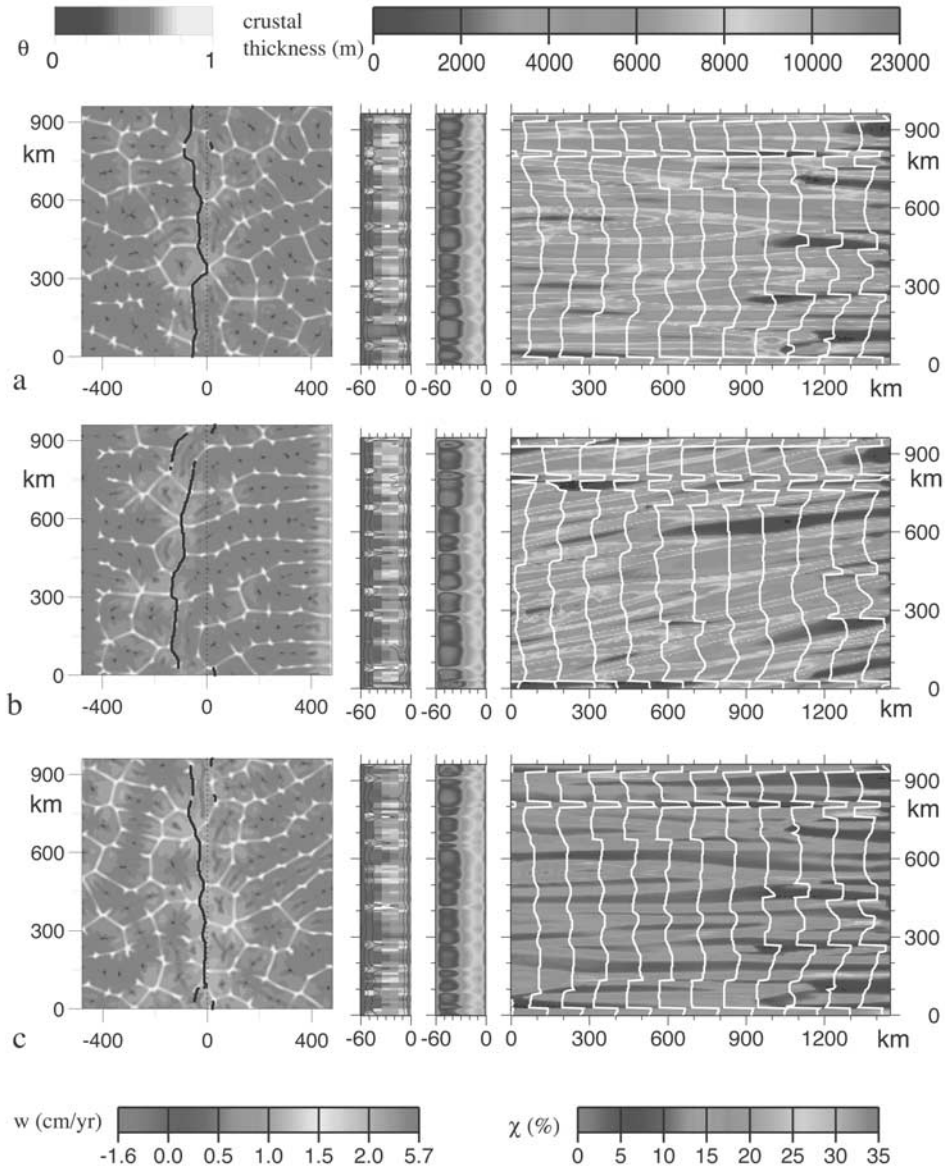

Figure 5. Three distinct experiments with a Ra = 90,000. Plotting conventions are as in Figure 2. The two first experiments (Figures 5a and 5b) are run with a half-spreading velocity V_{accr} = 17 mm yr^{-1}. They differ by the bottom shear velocity which is equal to $\mathbf{V}_{bot}$ = 0 and to $\mathbf{V}_{bot}$ = (8 mm yr^{-1}, 17 mm yr^{-1}) in Figures 5a and 5b, respectively. The experiment in Figure 5c shows the effect of doubling the spreading velocity: V_{accr} = 34 mm yr^{-1} instead of 17 mm yr^{-1} (here also $\mathbf{V}_{bot}$ = 0). The experiments in Figures 5a and 5b last 90 Myr, while the one in Figure 5c lasts 45 Myr. See color version of this figure at back of this issue.

$\mathbf{V}_{bot}$ = (8 mm yr^{-1}, 8 mm yr^{-1}), respectively. The Rayleigh number and the half-spreading velocity V_{accr} are still 30,000 and 17 mm yr^{-1}, respectively. The eastward or the south-eastward drift of the lower interface leads to a slow, westward migration of the ridge segments. After 90 Ma the ridge segments have been displaced by <100 km, i.e., with a velocity an order of magnitude lower than the eastward drift applied on the lower interface. The south-eastward drift of the lower interface leads to a small asymmetrical rotation of the Richter's roll on both sides of the ridge axis: anticlockwise along the eastern flank of the ridge and clockwise on its western flank. The magmatic lineations on the eastern flank of the plate now point to the south (Figure 4c). The obliquity of the lineations with respect to the spreading direction is consistent with the fact that the ridge-parallel bottom shearing moves the Richter's rolls in the flow direction. The westward drift of the ridge results from westward orientation, beneath the lithosphere, of the cavity flow driven by the eastward shear imposed at the bottom of the computing box (Figure 1).

3.3. Experiments With a Large Rayleigh Number

[27] In Figure 5 we present two models, with a Rayleigh number Ra of 90,000 and a top half-spreading velocity V_{accr} = 17 mm yr^{-1}. The bottom horizontal flow velocity is $\mathbf{V}_{bot}$ = 0 in the model of Figure 5a but $\mathbf{V}_{bot}$ = (17 mm yr^{-1},

8 mm yr^{-1}) in Figure 5b. In the former case, the convective cells form a polyhedral set of ascending hot sheets centered around an area of downwelling flow (Figure 5a). The number of hot sheets forming these polyhedrons varies and reaches a maximum of 8. Each individual hot sheet keeps a length of ~50–90 km and some polyhedrons exceed 150 km in diameter. Even after 90 Ma, the orientation of the various hot sheets remains independent of the spreading direction (Figure 5a). This is consistent with the fact that the convective velocity, which reaches a maximum of 60 mm yr^{-1}, is strong in comparison with the forced flow velocity, which reaches a maximum speed of only V_{accr} = 17 mm yr^{-1}. This convective structure is striking. For the same Rayleigh number range, standard Rayleigh-Benard convection displays two intersecting sets of rolls ~0.5D–0.7D in width and ~1D in length [*Frick et al.*, 1983]. Experiments run with exactly the same parameter values, but in which the diffuse flow resulting from plate accretion is omitted, also develop Richter's rolls 0.5D–0.7D in width (models not shown here, and *Rabinowicz et al.* [1993]). This suggests that it is the diffuse vertical bottom flow induced by the plate thickening which favors the development of the polyhedral flow structure. The ridge axis at the end of the experiment is almost continuous. The crustal lineations are separated by ~60 km (Figure 5b). The splitting or merging of magmatic lineations is common because of the numerous "pinched rolls" needed to give a polyhedral structure to the convective flow. The crustal production averaged over the whole experiment is 5.9 km. Initially, a large number of dipping currents develop beneath the ridge axis, explaining a relatively weak crustal production. After 40 Ma the crustal production is strong along the entire length of the ridge axis because the whole ridge is then located above ascending hot sheets of the polyhedral convective structure. The crustal production averaged along axis at the end of the experiment is 6.7 km. When the lower interface is sheared to the southeast, the flow still tends to display a polyhedral structure (Figure 5b). Strikingly, we see that along the eastern flank of the ridge, the spreading movement tends to destroy the polyhedrons and drives 100–140 km distant Richter's rolls, while over the western flank, the polyhedrons are clearly drawn (Figure 5b). This asymmetry results from the fact that when the lower interface is sheared in the direction of spreading, the cavity flow tends to increase the intensity of the shear stress due to spreading along the top boundary, while the opposite effect occurs when the shear acts in the opposite direction (see Figure 1). We also observe that the eastward shear of the lower interface leads to a slow westward drift of the ridge axis and that the southward bottom shear leads to a southward migration of the crustal production centers (Figure 5b). Otherwise, the mean crustal production remains the same as in the case with no bottom shearing (Figure 5a).

[28] In Figure 5c we display the results of an experiment similar to the one shown in Figure 5a (Ra = 90,000; no bottom shear, $\mathbf{V}_{bot}$ = 0) but with a faster half-spreading velocity, V_{accr} = 34 mm yr^{-1}. After 44 Myr of shearing at a spreading rate of 34 mm yr^{-1} the convective flow is very similar to the one after a shearing at a 17 mm yr^{-1} velocity during 90 Ma (Figures 5a and 5c). However, the mean crustal production is divided by ~2 when the plate spreading velocity doubles: 3.6 km at 34 mm yr^{-1} instead of the 5.9 km of mean crustal production at 17 mm yr^{-1}.

4. Discussion

4.1. Modeling Framework

[29] Although it is now commonly admitted that small-scale convection occurs in the partially molten mantle beneath the ridge, modeling this process is incredibly difficult. The reason is simple. The small-scale convection interacts strongly with the whole mantle flow and with the generation, percolation, and crystallization of the melt in the upper mantle. In fact, the problem becomes more tractable if we take into account the large amount of evidence showing that the partially molten domain has a viscosity drastically lower than that of the underlying mantle [*Rabinowicz et al.*, 1984; *Buck and Su*, 1989; *Sparks et al.*, 1993]. This implies that the small-scale mantle convection is "partially" confined within the mantle mush. Yet this confinement clearly cannot be complete. First, because of the oceanic plate accretion, material is sucked into the mantle mush. This process is extremely important because it provides the undepleted mantle from which the oceanic crust is extracted [*Scott*, 1992; *Turcotte and Phipps Morgan*, 1992; *Braun et al.*, 2000]. Also, part of the large-scale mantle flow driven by hot or cold spots circulates inside the mantle mush [*Schilling et al.*, 1995]. Here we consider that at some distance from hot and cold spots this flow corresponds to a horizontal and regionally constant temperature flow. As shown by *Vogt* [1976], this flow moves preferentially along the roof-shaped "valley" formed by the accreting oceanic plates. However, when the hot spot is located away from the ridge axis, the flow necessarily moves in a direction transverse to the valley. The mantle melting or crystallization being generated by heating/cooling or by compression/decompression, a large-scale horizontal flow with a locally constant temperature does not modify the melting rate. Consequently, the melting process occurs by decompression in the upwelling limbs of the small-scale cells. Meanwhile, the crystallization process occurs by cooling in the top boundary layer and by compression inside the downwelling limbs of the same convective cells. As shown above, these drastic approximations allow us to model the mantle dynamics with a tractable set of equations and boundary conditions.

4.2. Summary of the Main Results of the Modeling

[30] Although the cavity flow induced by the plate spreading tends to generate Richter's rolls ~200 km from the ridge plane, the convective circulation is clearly three-dimensional closer to the ridge axis. In fact, the 3-D nature of the flow results from the combined effects of the forced flows driven by plate spreading and plate accretion. Plate spreading generates a roof-shaped domain of quiescent flow around the ridge plane favoring the development of upwelling sheets there. The flow driven by plate accretion induces a slow and diffuse vertical flow at the bottom of the mantle mush which strongly enhances the buoyancy of the bottom convective boundary layer. The resulting dissymmetry between the bottom and top convective boundary layers leads to the development of cells with a polyhedral ascending flow structure [*White*, 1988]. The convective pattern below the ridge is a compromise between (1) Richter's rolls favored by plate spreading at some distance from the ridge,

(2) upwelling sheets along the ridge plane which develop because of the quiescence of the subridge flow at the bottom of the mush, and (3) polyhedrons favored by the diffuse upwelling flow driven by plate accretion.

[31] Clearly, the observed structures depend on (1) the Rayleigh number, (2) the spreading velocity, and (3) time. The time required to reach a quasi-steady state structure is almost independent of the Rayleigh number but decreases linearly with the half-spreading velocity. It is roughly equal to 90 and 45 Ma when $V_{accr} = 17$ and 34 mm yr^{-1}, respectively. Near the ridge axis, however, the convective pattern is governed by the Rayleigh number. A Rayleigh number of ~30,000 drives two orthogonal sets of rolls, parallel to the ridge axis and to the spreading direction, respectively. The characteristic width of the rolls increases with time. The length of the cells is ~70 km at the beginning of the experiment and reaches 110–150 km at the end. When the Rayleigh number reaches 90,000, the upwellings form polyhedrons with sides 50–90 km in length. In our formulation the ridge axis is free to move along the spreading direction and to adjust itself to the shear stresses generated along the lithosphere-mush interface by the convective circulation [*Rouzo et al.*, 1995]. During the transient period the ridge presents a discontinuous geometry with many U-shaped transform-ridge-transform systems. However, the ridge segments generally tend to realign to form a continuous line located above upwelling sheets of the convective circulation. Below the continuous portions of the ridge axis, the flow forms a set of connected sheets parallel to the ridge. Crustal production is twice as large at the intersection of these sheets as elsewhere along the ridge. Sometimes near a transient discontinuity, a ridge segment can sit temporally above a downwelling current. During this time the crustal production drops to zero along this ridge segment. In the synthetic maps of crustal thickness and isochrons the excess crustal production occurring above the intersection of two convective hot sheets produces magmatic lineations subparallel to the spreading direction (Figures 2–5). Yet two magmatic lineations often merge into one, or one lineation splits in two. These situations occur when the ridge axis lies over the intersection of three distinct hot ascending sheets. The component of large-scale mantle flow moving in a direction parallel to the ridge axis induces a southward migration of the hot upwelling sheets responsable for the crustal thickness variations. The resulting magmatic lineations form V shapes pointing in the direction of the large-scale flow. Yet a large-scale flow moving in a direction parallel to the spreading direction does not modify the convective structure. In fact, it only reinforces the shearing of the convective circulation by the oceanic plate which moves in the same direction. However, this flow component drives the ridge axis in the upstream direction. Note that both the segmentation and drift of the ridge axis induced by the convection in the mush and the shear of the large-scale mantle flow depend on the subridge local structure of convection and recirculation flow. This indicates that our results should remain invariant in a model taking into account the thinning of the mushy layer in the spreading direction.

[32] We have estimated the melting rates in the mantle and the crustal production at the ridge axis using the formalism of *McKenzie and Bickle* [1988]. The temperatures at the top and bottom of the models are adjusted to reach reasonable melting rates. At a depth of ~10 km inside the mantle mush, the melting fraction reaches a local maximum of 32%. Since we assume that the melt in excess of $m_c = 6\%$ is transported by porosity waves to the ridge axis, the resulting crust is a continuous mixture of melts derived from a parent rock whose melting rates range from 6 to 32% and melting depths range between 10 and 60 km below the bottom of the lithosphere. We have computed the mean melting rate and the averaged depth of melting along the whole ridge plane of model of Figure 5a (i.e., with a Rayleigh number $Ra = 90{,}000$, a top half-spreading velocity $V_{accr} = 17$ mm yr^{-1}, and a bottom velocity $\mathbf{V}_{bot} = 0$). This computation yields a mean melt rate of 16% and an averaged melting depth of 31.8 km. Since the top of the mush layer is assumed to be at 15 km below sea level, the average melting depth is at 46.8 km below sea level. These numbers agree with those estimated by *Langmuir et al.* [1992] and *Shen and Forsyth* [1995].

4.3. Evaluation of the Mean Crustal Thickness, the Rayleigh Number, and the Rate of Depletion of the Mantle Mush

[33] When the Rayleigh number rises from 30,000 to 90,000, with a half-spreading velocity $V_{accr} = 17$ mm yr^{-1}, the along-axis mean crustal thickness increases from 3.4 to 6.7 km. These numbers are upper bounds because they have been computed assuming that the mantle advected by the convective circulation is 100% fertile. This is the case when the bottom convective boundary layer is composed entirely of fertile mantle. Since this layer has a thickness of ~8 km and is fed with fertile mantle by the 1.1 mm yr^{-1} upward flow due to the plate accretion, it is completely filled with fertile mantle in ~7 Myr. To transport 100% of fertile mantle, the ascending flow along the ridge axis would have to be in contact during 7 Myr with the mush-dry mantle interface before moving upward. Because of the large viscosity contrast along the mush-mantle interface, the horizontal mean convective velocity close to this interface is slow. It is <10 mm yr^{-1} in the model with a Rayleigh number of 30,000 and twice as large in the model with a Rayleigh number of 90,000. Because of the 100–200 km extension of the convective cells it is likely that the convective current flowing along the 100-km-wide bottom interface of the convective cell remains in contact with this lower interface during the 7-Myr period required to fill it with fertile mantle. With a Rayleigh number of ~90,000, the convective upwelling provides 75% of fertile material below the ridge, enough to produce a crust 5 km thick on average. When the spreading rate doubles, the velocity of the upward flow due to the plate accretion also doubles. However, the melt flow rate reaching the lithosphere increases slowly because it mainly depends on the fertility rate and on the convective velocity. Thus the mean crustal production decreases by a factor of ~2. A factor of 3 increase of the Rayleigh number is required to double the convective velocity and to match the average 5 km mean crustal production.

[34] To produce a fixed crustal production, we therefore have two alternatives. Either we assume that the Rayleigh number of the mush layer is much greater than 90,000 and thus that most of the upwelling mantle flow below the ridge axis is composed of depleted material mixed with a constant flow of undepleted material, or we can assume that the

Rayleigh number varies around a value of 90,000 and that it is generally positively correlated with the spreading rate. We have shown above that the Rayleigh number depends mainly on the viscosity of the mush. Thus a variation by a factor of up to 10 in the Rayleigh number could be attributed to variations of a few tens of degrees of the bulk temperature of the mush layer. This estimate of the large-scale temperature variations below the ridge axis is reasonable if we consider that the mush is fed by large-scale convective flows. In the warmest domains the increase of the Rayleigh number increases the production of crust which consequently balances the crustal thinning expected at a faster spreading ridge. Therefore the invariant 5-km crustal thickness observed along most of the Earth's ridge system could result from the fact that the plate boundaries with the fastest spreading rates are those located above a mantle which is a few tens of degrees hotter. This conclusion agrees with global studies of the Earth's ridge system [*Lecroart et al.*, 1997]. Alternatively, if the second interpretation is correct, we can assume that the Rayeigh number of the mush is high in anomalously hot regions like the Icelandic hot spot and low at the Australia-Antarctic Discordance. Then our model can explain why the crustal production is clearly high while the spreading velocity is low at the Icelandic hot spot and why the crustal production is low above the cold though relatively fast spreading center of the Australia-Antarctic Discordance [*Forsyth et al.*, 1987; *Sempéré et al.*, 1991].

4.4. Stability of the Mantle Mush

[35] If we look at the partially molten mantle layer from below, we see a severe stability problem. In our models the mean temperature of the mush is 150°C lower than in the mantle below it. It is clear that the resulting negative buoyancy can be compensated by the positive buoyancy of the interstitial melt trapped in the upwelling flow. However, such an effect is not strong enough to ensure the overall stability or even the neutral stability of the whole layer. In other words, the 90 Myr stability of the mantle mush as a whole assumed in our modeling requires some justifications.

[36] The shear flow imposed at the bottom of the partially molten layer to simulate the coupling with the large-scale flow driven by whole mantle convection is consistent with a layering of the circulation on both sides of the bottom interface of the mush. If the hot spot plume penetrates inside the roof-shaped-mush layer, the resulting cavity flow will turn in a direction opposite to the one driven by mantle flow shearing the bottom interface of the mush. Accordingly, the sense of the ridge axis migration generated by the large-scale mantle flow depends dramatically on the stability of the mush layer. To achieve such stability requires a significant density contrast between the return flow and the overlying depleted mantle, which can only be due to compositional differences. Density contrasts attributable to chemical composition are essentially related to the Fe/Mg ratio of olivine and pyroxenes in the residual mantle depending themselves on the degree and pressure of melting. The higher the degree of melting, the lower the Fe/Mg ratio, and thus the density, of the residual mantle. For equal melting degrees the Fe/Mg ratio of the residue increases slightly as the pressure of melting increases [e.g., *Kinzler*, 1997]. The contrast in melting degree between hot spots and ridges is poorly constrained. Some authors have argued that higher crustal thicknesses at hot spots imply much more partial melting in mantle plumes than beneath mid-ocean ridges [*McKenzie and Bickle*, 1988; *White et al.*, 1992; *Langmuir et al.*, 1992]. This should be reflected in lava composition. Although slight differences in composition between hot spot lavas and mid-ocean ridge basalts (MORBs) exist, they can be attributed to pressure effects and to the dynamics of melt migration [*Liu and Chase*, 1991; *Ceuleneer et al.*, 1993; *Putirka*, 1999]. High crustal thicknesses at hot spots can also result from 3-D focusing of mantle flow [*Ribe and Christensen*, 1994]. The best guess is that the average melting degree is somewhat similar in both environments, particularly when the hot spot is located below a relatively thick lithosphere. There is no doubt, however, that the pressure of melting contrasts strongly. Accordingly, we can expect a residue richer in Fe, and hence denser material, in hot spots. Variations in the pressure of melting can also induce density contrasts in the residue related to mineralogy. The contribution of olivine and pyroxenes to the melt varies with pressure: the higher the pressure of melting, the higher the proportion of olivine entering in the melt phase, the lower the olivine/pyroxene ratio, and thus the density, of the residue [*Herzberg and Zhang*, 1996]. This effect will lower the density of the residual mantle in hot spots relative to ridges, an effect that will counteract and perhaps even balance the one related to the Fe/Mg ratio. In both ridge and hot spot settings, but particularly where a hot spot is overlain by a thick lithosphere, the melt extraction is not complete. Thus part of the melt will remain trapped in layers and eventually crystallize in layers as the temperature drops away from the upwelling currents. In the shallow environments (ridges) these layers will crystallize as pyroxenites and gabbroic cumulates with lower densities than the surrounding mantle [*Ceuleneer et al.*, 1996]. Below 50 km depth, they will crystallize as garnet pyroxenites and eclogites which are possibly 30% denser than the surrounding mantle [*Gregoire et al.*, 1994; *Kinzler*, 1997]. Near the bottom interface of the mush beneath a ridge axis, the flow advected by the hot spot should be rich in garnet pyroxenite and eclogite layers. We expect that these layers generate 1% of density contrast between the mush and underlying mantle. Such contrast in density is large enough to ensure the layering of the large-scale and small-scale convection on both sides of the bottom interface.

4.5. Modeling Perspectives

[37] Although we have tried to retain the essential physics known to act in the dynamics of the mantle mush, our modeling draws a partial picture of the geological situation because of the drastic simplifications needed to obtain a tractable set of equations. However, future work should be done to evaluate the effects of realistic rheological laws for the mantle mush, of melt percolation, and of crystallization. Also, future work should be concerned with the precise modeling of the interaction between small-scale convection in the mush and whole mantle convection.

5. Comparison Between Models and Data

[38] In this section we compare our numerical experiments to observations on the flanks of mid-ocean ridges presented by *Briais and Rabinowicz* [2002].

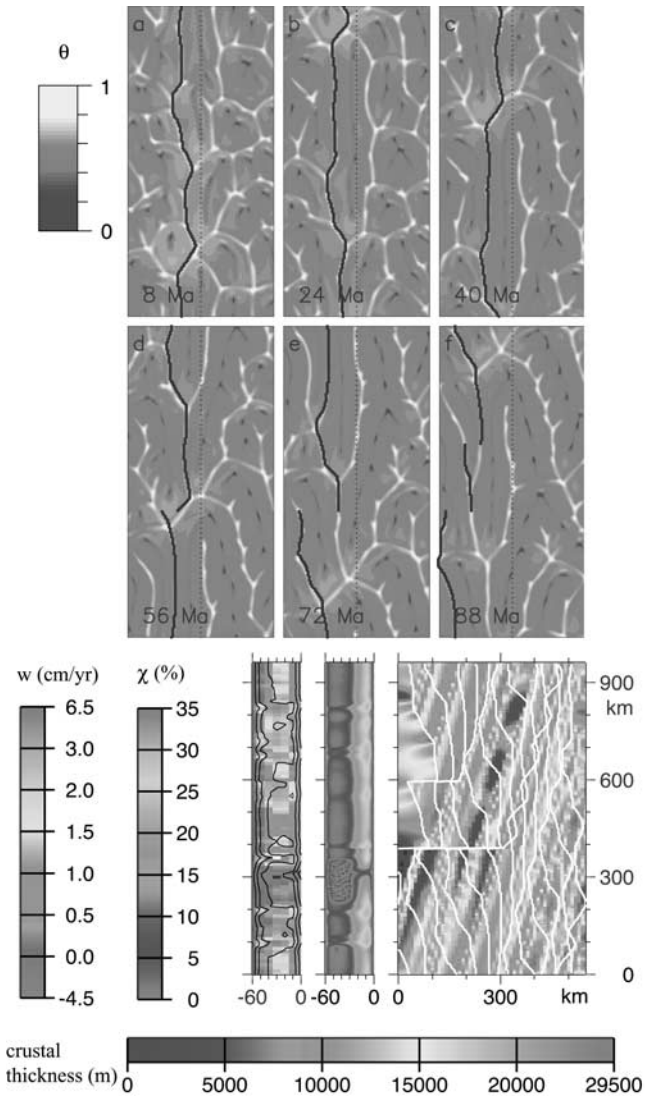

Figure 6. Mantle flow, isochrones, and magmatic lineations when a hot spot located beneath the ridge crest drives a very strong north-south mantle flow. Parameter values are those of the North Atlantic plates next to the Icelandic hot spot. The half-spreading velocity is 8.5 mm yr^{-1}. The Rayleigh number of the experiment Ra = 90,000. The bottom shear velocity $\mathbf{V}_{bot}$ = (0 mm yr^{-1}, 70 mm yr^{-1}). The experiment is initiated with the 90 Ma snapshot of the temperature field of Figure 5a experiment. (bottom left) The ridge plane isolines at the end of the experiment for vertical velocity w, temperature, and the melt fraction by weigh. (bottom right) The 90 Ma maps of the crustal lineations and isochrons. The crustal thickness is 13 km on average. (top) Several snapshots of the middepth temperature in a window restricted to the central part of the computing box. Note the development of major transform faults. Plotting conventions are as in Figure 2. See color version of this figure at back of this issue.

5.1. Along-Axis Variations of the Crustal Production and Segment Length

[39] Our model successfully predicts along-axis variations of the crustal production of the order of several kilometers. These variations define magmatic segments which are not always bounded by ridge offsets. The development of a ridge magmatic segmentation in the absence of an offset is an intrinsic characteristic of the model. Ridge segment centers are located above maxima of crustal thickness production because of favorable temperature and vertical velocity conditions (see along-axis sections in Figures 2–6). Crustal thickness average obtained for simulations with a half-spreading rate of 17 mm yr^{-1}, the average value for the southern Mid-Atlantic Ridge (MAR), and Ra of 30,000 or 90,000 are ~3.5 and ~6.7 km, respectively. The higher value is close to the 6-km average crustal thickness estimated for mid-ocean ridges [*Mutter and Mutter*, 1993]. The crustal thicknesses estimated in our model show variations in the range 0–20 km, larger than those estimated at mid-ocean ridges, which barely reach 5 km. One explanation for that discrepancy is that our model does not include any along-axis melt redistribution or crustal flow. These effects are suspected to occur at ridges, although their mechanism is not well documented [e.g., *Bell and Buck*, 1992; *Lawson et al.*, 1996].

[40] The resulting wavelength of the segmentation is ~110–150 km for Ra of 30,000 and 50–90 km for Ra of 90,000. For low Rayleigh numbers the upwellings correspond to intersections of convective rolls parallel to the ridge with the Richter rolls parallel to spreading. For higher Ra values the upwellings are located at the junctions of three to four polyhedral convective cells and are thus more closely spaced. The data analysis presented by *Briais and Rabinowicz* [2002] reveals that the ridge axis segment length is 50 km on average. Such a wavelength for the axial segmentation is closer to that obtained in our experiments with Ra of 90,000 than for the lower Ra. Segments of the northern Central Indian Ridge (CIR) are slightly shorter, but they are separated by large-offset transform faults, so that the distance between spreading cells is closer to 100 km. Our current model does not address the effect of transform faults on segment length or that of a strong obliquity between the ridge and the spreading direction. The easternmost section of the ultraslow spreading Southwest Indian Ridge has longer segments than average, reaching 130–200 km as estimated from mantle Bouguer gravity analysis [*Rommevaux-Jestin et al.*, 1997]. This region appears to be one of the coldest parts of that ridge and should be compared to our low-Ra experiments.

5.2. Evolution of the Segmentation Geometry

[41] In our model, series of segments develop above the upwelling sheets that are subparallel to the spreading ridge. Distinct series of segments located above two different upwelling sheets are usually separated by a large-offset discontinuity. Such discontinuities tend to be very stable in space, although the offset across them varies, whereas small offsets tend to migrate along axis. This contrast between two types of geometrical discontinuities is observed along the mid-ocean ridges, where transform faults tend to be stable enough to record the plate motion vector, whereas nontransform discontinuity traces are oblique to plate flow lines.

[42] The offsets between segments above the same upwelling sheet tend to decrease with time, so that at the

end of experiments representing 100 Myr of evolution, the ridge axis is almost a straight line, which is not observed in the oceans. In our model the evolution of the plate boundary geometry, or ''tectonic segmentation,'' obeys very simple laws depending only on the stresses developed in the thin axial lithosphere by the convective circulation. It does not take into account the complexities of the deformation of the young lithosphere near ridge axis discontinuities. It is likely that taking into account the rheology of the axial lithosphere may lead to a slightly slower realignment of the plate boundary geometry. Also, the kinematics of all plate boundaries have changed in the last 100 Myr, so that both the plate boundary and the upwelling convective sheets had to adjust to new conditions after each change in spreading direction. These kinematic changes explain part of the offsets of the plate boundaries.

[43] The rate at which the discontinuity offsets shrink in our model appears to depend both on the spreading rate and on the Rayleigh number: the higher the spreading rate, or the higher the Rayleigh number, the faster the ridge segments realign. This double effect is due to the adjustment of the convective rolls beneath the ridge axis, which is more efficient both at high spreading rates and at high *Ra*. The analysis of the oceanic data shows that along most of the intermediate spreading Southeast Indian and Pacific-Antarctic Ridges, the most characteristic discontinuities are small-offset overlapping spreading centers, which do not leave off-axis traces in the satellite gravity maps. Sections of slow spreading ridges affected by hot spots, such as the section of CIR near the Reunion/Rodrigues hot spot near 19°S, or the section of MAR near the Azores hot spot near 40°N, also have small-offset discontinuities. The observation that these sections of ridges are almost straight could be explained by the existence of a convective circulation with a relatively large Ra beneath the axis. Such sections of ridges are often limited by large transform faults which we infer could represent boundaries between independent zones of mantle flow with different Rayleigh numbers.

5.3. Evolution of the Magmatic Segmentation

[44] The lineations generated off-axis by the along-axis variations of crustal production tend to migrate, merge, and split, as they follow the hot upwellings of the mush flow. This is commonly observed on the flanks of mid-ocean ridges [*Grindlay et al.*, 1991; *Sloan and Patriat*, 1992; *Gente et al.*, 1995; *Briais and Rabinowicz*, 2002]. The along-axis migration is actually a characteristic of ''nontransform'' ridge axis discontinuities because their traces do not follow small circles of the Euler rotation between the plates, as transform faults usually do. The transient evolution of the convection in our model provides a plausible explanation for the migration of nontransform discontinuities. The lifetime of segments in our experiments is ~20–50 Myr. This is consistent with most of the observations [*Briais and Rabinowicz*, 2002]. On some sections of ridges, however, the segments can be followed only for 10 Myr. [e.g., *Gente et al.*, 1995]. This may be explained by several factors. First, changes in relative or absolute plate motion probably induce kinks in the magmatic lineations. Second, part of the evolution of the segmentation is probably controlled by the response of the lithosphere, which is not accounted for in our model. Third, the conditions of the extraction and distribution of the magma in the upwellings are not well known, let alone easy to include in a model. These three factors could also play a role in shaping the ridge segments, their discontinuities, and the detailed evolution of both. They should motivate further studies.

5.4. Influence of Hot or Cold Spots

[45] We introduce a simple shearing, or forced flow, at the base of the model box to simulate the interaction of the small-scale circulation beneath the ridge axis and the large-scale one due to hot or cold spots. Two prominent effects of the large-scale mantle flow on mid-ocean ridges are well accounted for by these experiments. First, the segments, and associated discontinuities, all migrate to follow the component of the large-scale flow parallel to the axis. The resulting lineations in the crustal thickness maps are oblique to the spreading direction but subparallel to each other. In other words, the segments do not tend to merge or split faster than in the experiments with no forced flow at depth, but the whole pattern drifts along with the large-scale flow. The tendency of magmatic segments to migrate away from hot spots or toward cold spots is well documented in the observations on the flanks of mid-ocean ridges [*Briais and Rabinowicz*, 2002]. For example, in the South Atlantic, segments are observed to migrate away from the Ascension, Santa Helena, Tristan da Cunha, and Discovery hot spots. On either side of the Australia-Antarctic Discordance, which appears to sit above a cold mantle spot [e.g., *Forsyth et al.*, 1987], propagators converge toward the discordance.

[46] The second effect is the drifting of the spreading system, including the ridge axis and the convective circulation beneath it, toward the origin of the large-scale flow. This accounts for the observation of asymmetric spreading along ridges with a hot spot on one of their flanks. Again, this is very prominent in the South Atlantic, where ridge asymmetries have affected the ridge at various epochs, probably under the influence of the Santa Helena, Tristan da Cunha, Discovery and Shona hot spots [*Müller et al.*, 1998; *Briais and Rabinowicz*, 2002]. It is also observed on the Central Indian Ridge between about 18°S and 20°S, closer to the Réunion/Rodrigues hot spot. In all cases, the ridge asymmetry is such that it tends to keep the ridge section closer to the hot spot than normal spreading and absolute plate motion would predict. Our results provide an explanation different from that of *Small* [1995], who attributes the spreading asymmetry to the weakness of the lithosphere on the hot spot side. A more careful analysis of the geophysical data in these environments is necessary to distinguish between the two possible effects.

[47] The effect due to the component of large-scale flow parallel to spreading is much slower than the effect due to the component parallel to the axis. In our experiments the rate of migration of the segments parallel to the ridge axis is similar to that of the large-scale flow, whereas the rate of drifting of the ridge system is an order of magnitude lower than the rate of the spreading-parallel flow. We infer that the two components of the flow from a hot spot interact in very different ways with the small-scale convective circulation beneath the ridge axis. The component parallel to the ridge axis simply entrains the entire small-scale convective system with it. The component of the large-scale flow parallel to spreading appears to have a less direct effect. As it shears

the bottom of the convective layer, the large-scale flow induces a cavity flow in the top half of the convective layer in the opposite sense (Figure 1). Because the ridge axis adjusts to the upwelling sheets just below it, the plate boundary tends to follow the return flow, that is, to get closer to the hot spot. The motion of the spreading system with respect to the hot spot therefore has a component controlled by the balance between the vigor of the hot spot flow and the spreading rate.

5.5. Evolution of the Ridge Around the Icelandic Hot Spot

[48] As suggested by *Vogt* [1971], the huge, subridge Icelandic hot spot likely induces a pipe flow inside the mantle mush corridor parallel to the ridge several thousands of kilometers away from Iceland, with an intensity largely exceeding the one generated by a hot spot several hundreds of kilometers away from the ridge. Two main characteristics of the Iceland hot spot–Mid-Atlantic Ridge interaction are, first, that the ridge kept a very low half-spreading velocity of $\sim$8 mm yr^{-1} during the last 60 Myr and, second, that the flow of the Icelandic hot spot is parallel to the ridge and reaches a velocity up to 10 times the half-spreading rate. Here we assume it is equal to 70 mm yr^{-1}. In Figure 6 we display the results of a simulation run with a Rayleigh number of 90,000, a half-spreading velocity of 8.5 mm yr^{-1}, and a bottom shear velocity $\mathbf{V}_{\mathrm{bot}}$ = (70 mm yr^{-1}, 0 mm yr^{-1}). The experiment is initiated with the 90 Ma snapshot of the temperature field of Figure 5a experiment. The polygonal set of upwelling sheets beneath the ridge crest which characterizes the initial condition of the experiment is rapidly transformed by the bottom shear flow. Now, because of the drastic difference of intensity between the hot spot shear flow and the plate-spreading one, the asymptotic structure of the small-scale convective flow consists in Richter's rolls whose axes are parallel to ridge. However, during most of the 90-Myr duration of the experiment, numerous old junctions between ascending sheets of the initial polyhedral flow persist. These junctions favor the transient development of branchings between different Richter's rolls. When the ridge follows one of these branchings, transform faults develop. The transform faults then connect different Richter's rolls. Finally, the transform offsets exceed 100 km and become permanent features. This evolution of the ridge axis geometry is specific to the intense flow of the Icelandic hot spot. It is striking to note how the ridge segmentation north of Iceland, characterized by large-offset transform faults between the northern Iceland rift, Kolbeinsey, Mohn's, and Knipovitch ridges, is reminiscent of Figure 6 [*Briais and Rabinowicz*, 2002]. Also, the 70 mm yr^{-1} southward shear flow drifts the subridge local heat anomalies at a similar speed. On the crustal map, 30-km-thick parallel lineations making a 60° angle with the spreading direction result from the along-axis transport of the junction line of hot sheets. These V-shaped lineations are the main characteristic of the Reykjanes ridge system. Our model provides an alternative explanation to that proposed by *Vogt* [1971] and *White et al.* [1995], which explains the V shape of the lineations south of Iceland by the advection below the ridge of thermal instabilities taking birth inside the axis of the mantle plume.

Appendix A: Calculation of the Elastic Stresses on the Overriding Lithosphere

[49] Along the lithosphere-plastic mantle interface, convection induces a normal stress $G(x, y)$ and a horizontal shear of components $SH_x(x, y)$ and $SH_y(x, y)$ along the x and y direction, respectively. These functions verify

$$G(x,y) = -p(x,z,z=0) + 2\eta\frac{dw}{dz}(x,y,z=0), \tag{A1}$$

$$SH_x(x,y) = \eta\frac{du}{dz}(x,y,z=0), \tag{A2}$$

$$SH_y(x,y) = \eta\frac{dv}{dz}(x,y,z=0), \tag{A3}$$

where P and u, v, w are the pressure and velocity fields calculated at the top ($z = 0$) of the convective model. Let h be the thickness of the elastic plate and z be the vertical coordinate pointing downward and originating along the midhorizontal plane of the elastic plate. The shear along the top horizontal interface of the plate is zero ($z = -h/2$ plane). In fact, we can decompose the shear acting on both the top and bottom horizontal face of the plate as the superposition of a "torque field" and a "stretching field." The torque field is equal to ($SH_x(x, y)/2$, $SH_y(x, y)/2$) along the top and bottom horizontal interfaces of the plate (z = + or $-h/2$ planes). The stretching field is $-(SH_x(x, y)/2, SH_y(x, y)/2)$ and $+(SH_x(x, y)/2, SH_y(x, y)/2)$ along the top and bottom interfaces of the plate, respectively. The torque field corresponds to a moment of rotation along the y and x axes, respectively. It induces a vertical deflexion of the plate ξ and two rotations of angle $\partial\xi/\partial x$ and $\partial\xi/\partial y$ along the y and x axes, respectively. Using the same approximations as those used to quantify the plate deflection due to an island load, we easily verify that ξ is solution of [*Turcotte and Schubert*, 1982]

$$\frac{Eh^3\Delta^2\xi}{12(1-\nu)} + (\rho_m - \rho_w)\xi = G + \left(\frac{\partial SH_x}{\partial x} + \frac{\partial SH_y}{\partial y}\right), \tag{A4}$$

where E and ν designate the Young modulus and the Poisson coefficient of the plate, ρ_w is the seawater density, and

$$\Delta = \frac{\partial^2}{\partial x^2} + \frac{\partial^2}{\partial y^2}. \tag{A5}$$

Also the stress field inside the plate verifies

$$\sigma_{xx} = -\frac{zE}{(1-\nu^2)}\left(\frac{\partial^2\xi}{\partial x^2} + \nu\frac{\partial^2\xi}{\partial y^2}\right), \tag{A6}$$

$$\sigma_{yy} = -\frac{zE}{(1-\nu^2)}\left(\frac{\partial^2\xi}{\partial y^2} + \nu\frac{\partial^2\xi}{\partial x^2}\right), \tag{A7}$$

$$\partial_{xy} = -\frac{zE}{(1+\nu)}\frac{\partial_2\xi}{\partial x\partial y}. \tag{A8}$$

The sign of the stress components changes on both sides of the central plane. Thus, either the lower part or the upper part of the plate is under horizontal compression. Fractures at the ridge axis result from hydraulic fracturing of the sheeted dike complex. Thus the torque field cannot contribute to the

vertical fracturing of the lithosphere at the ridge axis, since the stress field favors fracturing on one half of the plate section and disfavors it along the other half. Hence we see that the ''torque stress field'' generated by the sublithospheric convective circulation does not have a direct contribution on the lithospheric fracturing at the ridge crest. Accordingly, we will assume here that it makes no contribution to the ridge segmentation and migration process.

[50] The shear vectors of the stretching field along the top and bottom of the elastic plate point in the same horizontal direction. Both forces tend to stretch or compress the elastic plate along the same horizontal direction. This stress field induces a displacement field which can be assumed to be strictly horizontal in a first approximation. Let, $t_x(x, y)$ and $t_y(x, y)$ be the components of this field along the x and y direction, respectively. Now, the thin plate approximation implies that the stress components of the tensor field in the elastic plate verify

$$\sigma_{zz} \approx \sigma_{xz} \approx \sigma_{yz} \ll \sigma_{xy} \approx \sigma_{xx} \approx \sigma_{yy}, \tag{A9}$$

$$\sigma_{xy} = \frac{E}{2(1+\nu)}\left(\frac{\partial t_x}{\partial y} + \frac{\partial t_y}{\partial x}\right), \tag{A10}$$

$$\sigma_{xx} = \frac{E}{(1-\nu^2)}\left(\frac{\partial t_x}{\partial x} + \nu\frac{\partial t_y}{\partial y}\right), \tag{A11}$$

$$\sigma_{yy} = \frac{E}{(1-\nu^2)}\left(\frac{\partial t_y}{\partial y} + \nu\frac{\partial t_x}{\partial x}\right). \tag{A12}$$

Let us assume that the shearing stresses in the plates induced by the stretching field verify

$$\sigma_{xz} = zSH_x/h \tag{A13}$$

$$\sigma_{yz} = zSH_y/h. \tag{A14}$$

Then using the two following equations of equilibrium:

$$\frac{\partial \sigma_{xx}}{\partial x} + \frac{\partial \sigma_{xy}}{\partial y} + \frac{\partial \sigma_{xz}}{\partial z} = 0, \tag{A15}$$

$$\frac{\partial \sigma_{yx}}{\partial x} + \frac{\partial \sigma_{yy}}{\partial y} + \frac{\partial \sigma_{yz}}{\partial z} = 0, \tag{A16}$$

we deduce that

$$\frac{(1-\nu)}{2}\frac{\partial^2 t_x}{\partial y^2} + \frac{(1+\nu)}{2}\frac{\partial^2 t_y}{\partial x \partial y} + \left(1-\nu^2\right)\frac{SH_x}{hE} = 0 \tag{A17}$$

$$\frac{\partial^2 t_y}{\partial y^2} + \frac{(1-\nu)}{2}\frac{\partial^2 t_y}{\partial x^2} + \frac{(1+\nu)}{2}\frac{\partial^2 t_x}{\partial x \partial y} + \left(1-\nu^2\right)\frac{SH_y}{hE} = 0. \tag{A18}$$

Separation of the variables yields

$$\Delta^2 t_x + \frac{2(1+\nu)}{Eh}\left(\frac{\partial^2 SH_x}{\partial y^2} + \frac{(1-\nu)}{2}\frac{\partial^2 SH_x}{\partial y^2}\right) - \frac{(1+\nu)^2}{Eh}\frac{\partial^2 SH_y}{\partial x \partial y} = 0 \tag{A19}$$

$$\Delta^2 t_y + \frac{2(1+\nu)}{Eh}\left(\frac{\partial^2 SH_y}{\partial x^2} + \frac{(1-\nu)}{2}\frac{\partial^2 SH_y}{\partial y^2}\right) - \frac{(1-\nu)^2}{Eh}\frac{\partial^2 SH_x}{\partial x \partial y} = 0. \tag{A20}$$

[51] Both (A19) and (A20) are solved by Fourier transform. In the numerical models, the ridge crest position is moved along the spreading direction, at a velocity of $V_{accr}/2$ in order to superpose it on the local maximum of the normal stress $\sigma_{xx}(x,y)$ in the elastic plate induced by the (t_c,t_y) displacement field.

[52] **Acknowledgments.** The initiation of this work benefited from discussions with and suggestions by Jean Christophe Sempéré and Stephane Rouzo. Also, Georges Ceuleneer, Fabien Dubuffet, Kurt Feigl, and Marc Monnereau greatly improved the present modeling and manuscript.

References

Barnouin-Jha, K., E. M. Parmentier, and D. W. Sparks, Buoyant mantle upwelling and crustal production at oceanic spreading centers: On-axis segmentation and off-axis melting, *J. Geophys. Res.*, *102*, 11,979–11,989, 1997.

Bell, R. E., and W. R. Buck, Crustal control of ridge segmentation inferred from observations of the Reykjanes Ridge, *Nature*, *357*, 583–586, 1992.

Blankenbach, B., et al., A benchmark comparison for mantle convection codes, *Geophys. J. Int.*, *98*, 23–38, 1989.

Braun, M. G., G. Hirth, and E. M. Parmentier, The effect of deep damp melting on mantle flow and melt generation beneath mid ocean ridges, *Earth Planet. Sci. Lett.*, *176*, 339–356, 2000.

Briais, A., and M. Rabinowicz, Temporal variations of the segmentation of slow to intermediate spreading mid-ocean ridges, 1, Synoptic observations based on satellite altimetry data, *J. Geophys. Res.*, 10.1029/2001JB000533, in press, 2002.

Buck, R., and W. Su, Focused mantle upwelling below mid-ocean ridges due to feedback between viscosity and melting, *Geophys. Res. Lett.*, *16*, 641–644, 1989.

Busse, F. H., and J. A. Whitehead, Oscillatory and collective instabilities in large Prandtl number convection, *J. Fluid Mech.*, *47*, 305–320, 1974.

Cathles, L. M., *The Viscosity of the Earth's Mantle*, Princeton Univ. Press, Princeton, N. J., 1975.

Ceuleneer, G., and M. Rabinowicz, Mantle flow and melt migration beneath oceanic ridges: Models derived from observations in ophiolites, in *Mantle Flow and Melt Generation at Mid-ocean Ridges*, *Geophys. Monogr. Ser.*, vol. 71, edited by J. Phipps Morgan, D. K. Blackman, and J. M. Sinton, pp. 72–154, AGU, Washington, D. C., 1992.

Ceuleneer, G., M. Monnereau, M. Rabinowicz, and C. Rosemberg, Thermal and petrological consequences of melt migration within mantle plumes, *Philos. Trans. R. Soc. London, Ser. A*, *342*, 53–64, 1993.

Ceuleneer, G., M. Monnereau, and I. Amri, Thermal structure of a fossil mantle diapir inferred from the distribution of mafic cumulates, *Nature*, *379*, 149–153, 1996.

Choblet, G., and E. M. Parmentier, Mantle upwelling and melting beneath slow spreading centers: Effects of variable rheology and melt productivity, *Earth Planet. Sci. Lett.*, *184*, 589–604, 2001.

Christensen, U., and U. Harder, 3-D convection with variable viscosity, *Geophys. J. Int.*, *104*, 213–226, 1991.

Connolly, J. A. D., and Y. Y. Podladchikov, Compaction-driven fluid flow in viscoelastic rock, *Geodin. Acta*, *11*, 55–84, 1998.

Daines, N. J., and D. L. Kohlstedt, Influence of deformation on melt topology in peridotites, *J. Geophys. Res.*, *102*, 10,257–10,271, 1997.

Douglas, J., and G. G. Rachford, On the numerical solution of heat conduction problems in two and three space variables, *Trans. Am. Math. Soc.*, *82*, 421–439, 1956.

Dubuffet, F., M. Rabinowicz, and M. Monnereau, Multiple-scales in mantle convection, *Earth Planet. Sci. Lett.*, *178*, 351–356, 2000.

Forsyth, D. W., R. L. Ehrenbard, and S. Chapin, Anomalous upper mantle beneath the Australia-Antarctic Discordance, *Earth Planet. Sci. Lett.*, *84*, 471–478, 1987.

Frick, H., F. Busse, and R. M. Clever, Steady three-dimensional convection at high Prandtl number, *J. Fluid Mech.*, *127*, 141–163, 1983.

Gente, P., R. Pockalny, C. Durnd, C. Deplus, M. Maia, G. Ceuleneer, C. Mével, M. Cannat, and C. Laverne, Characteristics and evolution of the segmentation of the Mid-Atlantic Ridge between 20°N and 24°N during the last 10 million years, *Earth and Planet. Sci. Lett.*, *129*, 55–71, 1995.

Ghods, A., and J. Harkani-Hamed, Melt migration beneath mid-ocean ridges, *Geophys. J. Int.*, *140*, 687–697, 2000.
Gregoire, M., N. Mattielli, C. Nicollet, J.-Y. Cottin, H. Leyrit, D. Weis, N. Shimizu, and A. Giret, Oceanic mafic granulite xenoliths from the Kerguelen archipelago, *Nature*, *367*, 360–363, 1994.
Grindlay, N. R., P. J. Fox, and K. C. Macdonald, Second-order ridge axis discontinuities in the South Atlantic: Morphology, structure and evolution, *Mar. Geophys. Res.*, *13*, 21–50, 1991.
Herzberg, C., and J. Zhang, Melting experiments on anhydrous peridotite KLB-1: Compositions of magmas in the upper mantle and transition zone, *J. Geophys. Res.*, *101*, 8271–8295, 1996.
Hirth, G., and D. L. Kohlstedt, Experimental constraints on the dynamics of the partially molten upper mantle: Deformation in the diffusion creep regime, *J. Geophys. Res.*, *100*, 1981–2001, 1995.
Ito, G., Y. Shen, G. Hirth, and C. J. Wolfe, Mantle flow, melting and dehydration of the Iceland mantle plume, *Earth Planet. Sci. Lett.*, *165*, 81–96, 1999.
Jarvis, G. T., and D. P. McKenzie, Convection in a compressible fluid with an infinite Prandtl number, *J. Fluid Mech.*, *96*, 515–583, 1980.
Jha, K., E. M. Parmentier, and J. Phipps Morgan, The role of mantle-depletion and melt retention in spreading center segmentation, *Earth Planet. Sci. Lett.*, *125*, 221–234, 1994.
Jull, M., and D. McKenzie, The effect of deglaciation on mantle melting beneath Iceland, *J. Geophys. Res.*, *101*, 21,815–21,828, 1996.
Khodakovskii, G., M. Rabinowicz, G. Ceuleneer, and V. Trubitsyn, Melt percolation in a partially molten mantle mush: Effect of a variable viscosity, *Earth Planet. Sci. Lett.*, *134*, 267–281, 1995.
Khodakovskii, G., M. Rabinowicz, P. Genthon, and G. Ceuleneer, 2D modeling of melt percolation in the mantle: The role of a melt-dependent mush viscosity, *Geophys. Res. Lett.*, *25*, 683–686, 1998.
Kinzler, R. J., Melting of mantle temperature at pressures approaching the spinel to garnet transition: Application to mid-ocean ridge basalt petrogenesis, *J. Geophys. Res.*, *102*, 853–874, 1997.
Langmuir, C. H., E. M. Klein, and T. Plank, Petrological systematics of mid-ocean ridge basalts: Constraints on melt generation beneath ocean ridges, in *Mantle Flow and Melt Generation at Mid-ocean Ridges*, *Geophys. Monogr. Ser.*, vol. 71, edited by J. Phipps Morgan, D. K. Blackman, and J. M. Sinton, pp. 18–280, AGU, Washington, D. C., 1992.
Lawson, K., R. C. Searle, J. A. Pearce, P. Browning, and P. Kempton, Detailed volcanic geology of the MARNOK area, Mid-Atlantic Ridge north of Kane transform, in *Tectonic, Magmatic, Hydrothermal and Biological Segmentation of Mid-ocean Ridges*, edited by C. J. MacLeod, P. A. Tyler, and C. L. Walker, *Geol. Soc. Spec. Publ., 118*, 6–102, 1996.
Lecroart, P., A. Cazenave, Y. Ricard, C. Thoraval, and D. G. Pyle, Along axis dynamic topography constrained by major-element chemistry, *Earth Planet. Sci. Lett.*, *149*, 49–56, 1997.
Liu, M., and C. G. Chase, Evolution of Hawaiian basalts: A hotspot melting model, *Earth Planet. Sci. Lett.*, *104*, 151–165, 1991.
McKenzie, D., and M. J. Bickle, The volume and composition of melt generated by extension of the lithosphere, *J. Petrol.*, *29*, 625–679, 1988.
MELT Seismic Team, Imaging the deep seimic structure beneath a mid-ocean ridge: The MELT experiment, *Science*, *280*, 1215–1218, 1998.
Monnereau, M., M. Rabinowicz, and E. Arquis, Mechanical erosion and reheating of the lithosphere: A numerical model for hotspot swells, *J. Geophys. Res.*, *98*, 809–823, 1993.
Müller, R. D., W. R. Roest, and J.-Y. Royer, Asymmetric sea-floor spreading caused by ridge-plume interactions, *Nature*, *396*, 455–459, 1998.
Mutter, C. Z., and J. C. Mutter, Variations in thickness of layer 3 dominate oceanic crust structure, *Earth Planet. Sci. Lett.*, *117*, 295–317, 1993.
Parmentier, E. M., and J. Phipps Morgan, Spreading rate dependence of three-dimensional structure in oceanic spreading centres, *Nature*, *348*, 325–328, 1990.
Parmentier, E. M., D. L. Turcotte, and K. E. Torrance, Studies of finite amplitude non-Newtonian convection with applications to convection in the Earth's mantle, *J. Geophys. Res.*, *81*, 1839–1846, 1976.
Parsons, B., and J. B. Sclater, An analysis of the variation of the ocean floor bathymetry and heat flow with age, *J. Geophys. Res.*, *82*, 803–827, 1977.
Phipps Morgan, J., and M. E. Parmentier, Crenulated seafloor: Evidence for spreading-rate dependent structure of mantle upwelling and melting beneath a mid-oceanic spreading center, *Earth Planet. Sci. Lett.*, *129*, 73–84, 1995.
Putirka, K., Melting depths and mantle heterogeneity beneath Hawaii and the East Pacific Rise: Constraints from Na/Ti and rare earth element ratios, *J. Geophys. Res.*, *104*, 2817–2829, 1999.
Rabinowicz, M., A. Nicolas, and J.-L. Vigneresse, A rolling mill effect in asthenosphere beneath oceanic spreading centers, *Earth Planet. Sci. Lett.*, *67*, 97–108, 1984.
Rabinowicz, M., G. Ceuleneer, M. Monnereau, and C. Rosemberg, Three-dimensional models of mantle flow across a low-viscosity zone: Implications for hotspot dynamics, *Earth Planet. Sci. Lett.*, *99*, 170–184, 1990.
Rabinowicz, M., S. Rouzo, J.-C. Sempéré, and C. Rosemberg, Three-dimensional mantle flow beneath mid-ocean ridges, *J. Geophys. Res.*, *98*, 7851–7869, 1993.
Rabinowicz, M., P. Genthon, G. Ceuleneer, and M. Hillairet, Compaction in a mantle mush with high melt concentrations and the generation of magma chambers, *Earth Planet. Sci. Lett.*, *188*, 313–328, 2001.
Ribe, N. M., and U. Christensen, Three-dimensional modeling of plume lithosphere interaction, *J. Geophys. Res.*, *99*, 669–682, 1994.
Ricard, Y., and B. Wuming, Inferring viscosity and the 3-D density structure of the mantle from geoid, topography and plate velocities, *Geophys. J. Int.*, *105*, 561–572, 1991.
Richter, F. M., and B. Parsons, On the interaction of two scales of convection in the mantle, *J. Geophys. Res.*, *80*, 2629–2681, 1975.
Robinson, E. M., and B. Parsons, The effect of a shallow low viscosity layer in the apparent compensation of mid-plate swells, *J. Geophys. Res.*, *93*, 3144–3156, 1988.
Rommevaux-Jestin, C., C. Deplus, and P. Patriat, Mantle Bouguer anomaly along an ultra slow-spreading ridge: Implications for accretionary processes and comparison with results from central Mid-Atlantic Ridge, *Mar. Geophys. Res.*, *19*, 481–503, 1997.
Rouzo, S., M. Rabinowicz, and A. Briais, Segmentation of mid-ocean ridges with an axial valley induced by small-scale mantle convection, *Nature*, *374*, 795–798, 1995.
Schilling, J. G., C. Ruppel, A. N. Davis, B. McCully, S. A. Tighe, R. H. Kingsley, and J. Lin, Thermal structure of the mantle beneath the equatorial Mid-Atlantic Ridge: Inferences from the spatial variation of dredged basalt glass compositions, *J. Geophys. Res.*, *100*, 10,057–10,076, 1995.
Scott, D. R., Small scale convection and mantle melting beneath mid-ocean ridges, in *Mantle Flow and Melt Generation at Mid-ocean Ridges*, *Geophys. Monogr. Ser.*, vol. 71, edited by J. Phipps Morgan, D. K. Blackman, and J. M. Sinton, pp. 31–327, AGU, Washington, D. C., 1992.
Scott, D. R., and D. Stevenson, Magma ascent by porous flow, *J. Geophys. Res.*, *91*, 9283–9296, 1986.
Scott, D. R., and D. J. Stevenson, A self-consistent model of melting, magma migration and buoyancy-driven circulation beneath mid-ocean ridges, *J. Geophys. Res.*, *94*, 2973–2988, 1989.
Sempéré, J.-C., J. Palmer, D. Christie, J. Phipps Morgan, and A. Shor, The Australian-Antarctic discordance, *Geology*, *19*, 429–432, 1991.
Shen, Y., and D. W. Forsyth, Geochemical constraints on initial and final depths of melting beneath mid-ocean ridges, *J. Geophys. Res.*, *100*, 2211–2237, 1995.
Sloan, H., and P. Patriat, Kinematics of the North American–African plate boundary between 28° and 29° during the last 10 Ma: Evolution of the axial geometry and spreading rate, *Earth Planet. Sci. Lett.*, *113*, 323–341, 1992.
Small, C., Observations of ridge-hotspot interactions in the Southern Ocean, *J. Geophys. Res.*, *100*, 17,931–17,946, 1995.
Smaltzl, J., G. A. Houseman, and U. Hansen, Mixing properties of three-dimensional (3D) stationary convection, *Phys. Fluids*, *7*, 1027–1033, 1995.
Sotin, C., and M. Parmentier, Dynamical consequences of compositional and thermal density stratification beneath spreading centers, *Geophys. Res. Lett.*, *16*, 835–838, 1989.
Sparks, D. W., E. M. Parmentier, and J. Phipps Morgan, Three-dimensional mantle convection beneath a segmented spreading center: Implications for along-axis variations in crustal thickness and gravity, *J. Geophys. Res.*, *98*, 21,977–21,996, 1993.
Spiegelman, M., Flow in deformable porous media, II, Numerical analysis-the relationship between shock waves and solitary waves, *J. Fluid Mech.*, *247*, 39–63, 1993.
Spiegleman, M., and J. Elliot, Consequences for melt transport for U-series disequilibrium in young lavas, *Earth Planet. Sci. Lett.*, *118*, 1–20, 1993.
Stevenson, D. J., Spontaneous small-scale melt segregation in partial melts undergoing deformation, *Geophys. Res. Lett.*, *16*, 1067–1070, 1989.
Turcotte, D. L., and J. Phipps Morgan, The physics of magma migration and mantle flow beneath a Mid-ocean ridge, in *Mantle Flow and Melt Generation at Mid-ocean Ridges*, *Geophys. Monogr. Ser.*, vol. 71, edited by J. Phipps Morgan, D. K. Blackman, and J. M. Sinton, pp. 15–182, AGU, Washington, D. C., 1992.
Turcotte, D. L., and G. Schubert, *Geodynamics: Applications of Continuum Physics to Geological Problems*, 450 pp., John Wiley, New York, 1982.
Vogt, P. R., Asthenosphere motion recorded by the ocean floor south of Iceland, *Earth Planet. Sci. Lett.*, *13*, 153–160, 1971.
Vogt, P. R., Plumes, sub-axial pipe flow and topography along the mid-ocean ridges, *Earth Planet. Sci. Lett.*, *29*, 309–325, 1976.
Watson, S., and D. McKenzie, Melt generation by plumes: A study of Hawaiian volcanism, *J. Petrol.*, *32*, 501–537, 1991.
Webb, S. C., and D. W. Forsyth, Structure of the upper mantle under the

EPR from waveform inversion of regional events, *Science*, *280*, 1227–1229, 1998.

White, D. B., The planform and onset of convection with a temperature-dependent viscosity, *J. Fluid Mech.*, *191*, 247–286, 1988.

White, R. S., D. McKenzie, and R. K. O'Nions, Oceanic crustal thickness from seismic measurements and rare earth element inversions, *J. Geophys. Res.*, *97*, 19,683–19,715, 1992.

White, R. S., J. W. Bown, and J. R. Smallwood, The temperature of the Iceland plume and origin of outward-propagating V-shaped ridges, *J. Geol. Soc. London*, *152*, 1039–1045, 1995.

Whitehead, J., and B. Parsons, Observations of convection at Rayleigh number up to 760,000 in a fluid with large Prandtl number, *Geophys. Astrophys. Fluid Dyn.*, *9*, 201–217, 1978.

Whitehead, J. A., H. J. B. Dick, and H. Schouten, A mechanism for magmatic accretion under spreading centers, *Nature*, *312*, 146–148, 1984.

Wiggins, C., and M. Spiegelman, Magma migration and magmatic solitary waves in 3-D, *Geophys. Res. Lett.*, *22*, 1289–1292, 1995.

A. Briais, Laboratoire d'Etudes en Géophysique et Océanographie Spatiales, CNRS, UMR 5566, Observatoire Midi-Pyrénées, 14, Avenue Edouard Belin, F-31400 Toulouse, France. (Anne.Briais@cnes.fr)

M. Rabinowicz, Laboratoire de Dynamique Terrestre et Planétaire, UMR 5562, Observatoire Midi-Pyrénées, 14, Avenue Edouard Belin, F-31400 Toulouse, France. (Michel.Rabinowicz@cnes.fr)

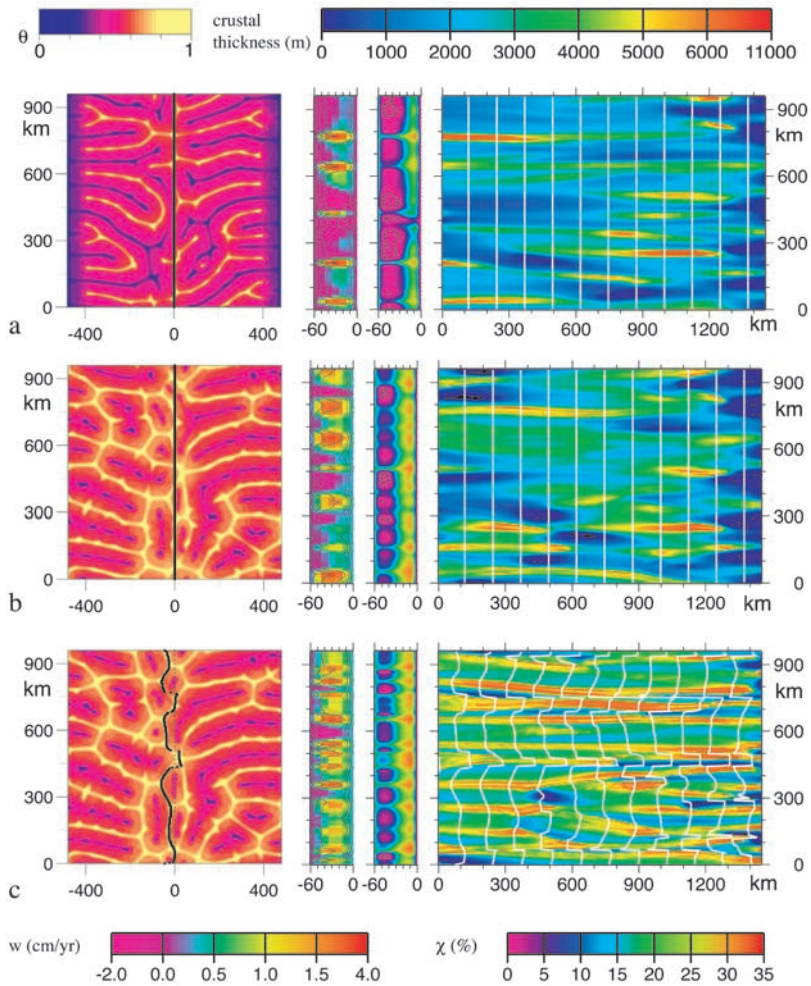

Figure 2. Comparison of three distinct, 90-Myr-long experiments with a Ra = 30,000, a half-spreading velocity V_{accr} = 17 mm yr^{-1} and a bottom shear $\mathbf{V}_{bot}$ = 0. In the first two experiments the ridge axis position is fixed (Figures 2a and 2b), while in the last one it migrates as explained in the text and Appendix A (Figure 2c). In the first model the upwelling driven by plate accretion is not added to the flow field (Figure 2a). The maps at the left represent the final snapshot of the middepth horizontal nondimensional thermal field, bright colors designate hot fluids with close to 1, and dark ones designate cold fluids with close to 0. The initial position of the axis is marked by a north-south dotted line and the final position by solid lines. (right) Isochron and crustal thickness on the eastern flank of the oceanic plate. The isochrons at 8 Myr-interval are drawn in plain white lines, and the crustal thickness is in color. Scales of color for the crustal maps are drawn at the top. The middle left box shows vertical velocity w in the ridge plane and temperature at the end of each experiment. Isotherms are drawn in plain black lines. The middle right box displays melt fraction by weigh along the ridge plane. Color scales for w and for are shown at the bottom.

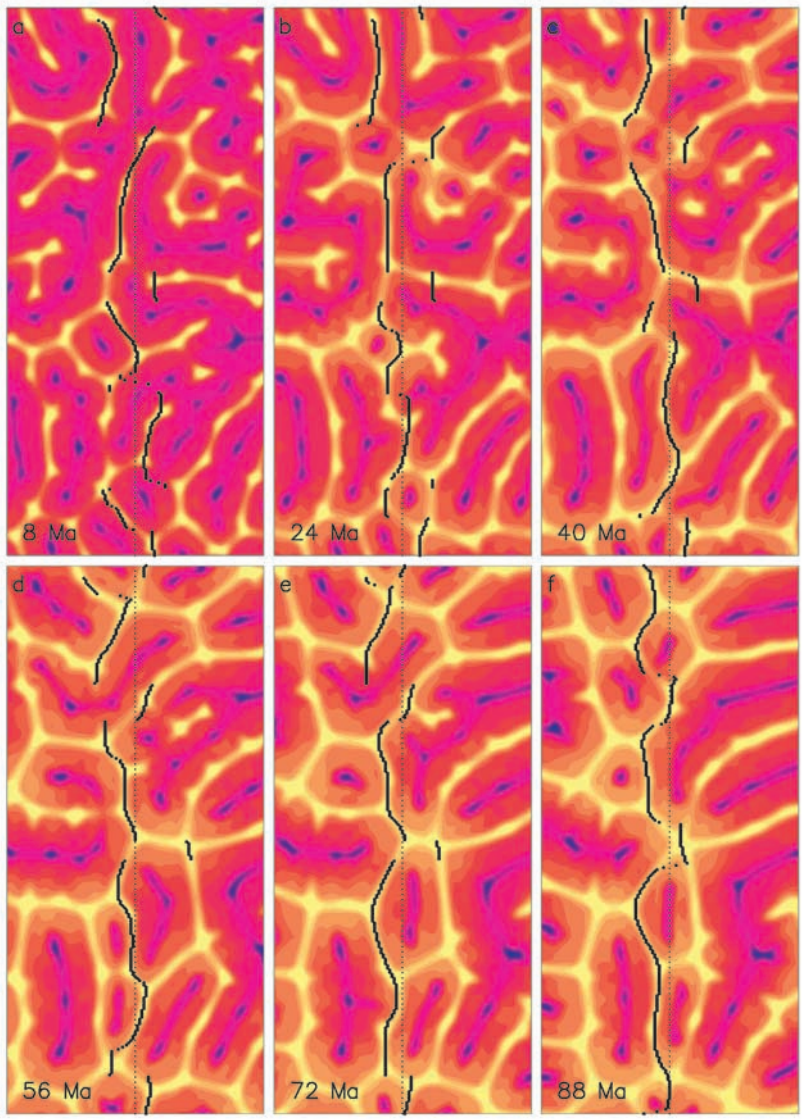

Figure 3. Evolution of the thermal field when Ra = 30,000, V_{accr} = 17 mm yr^{-1}, and $\mathbf{V}_{bot}$ = 0 (model also shown in Figure 2c), shown as snapshots of the middepth temperature in a window restricted to the central part of the computing box. Plotting conventions are as in Figure 2.

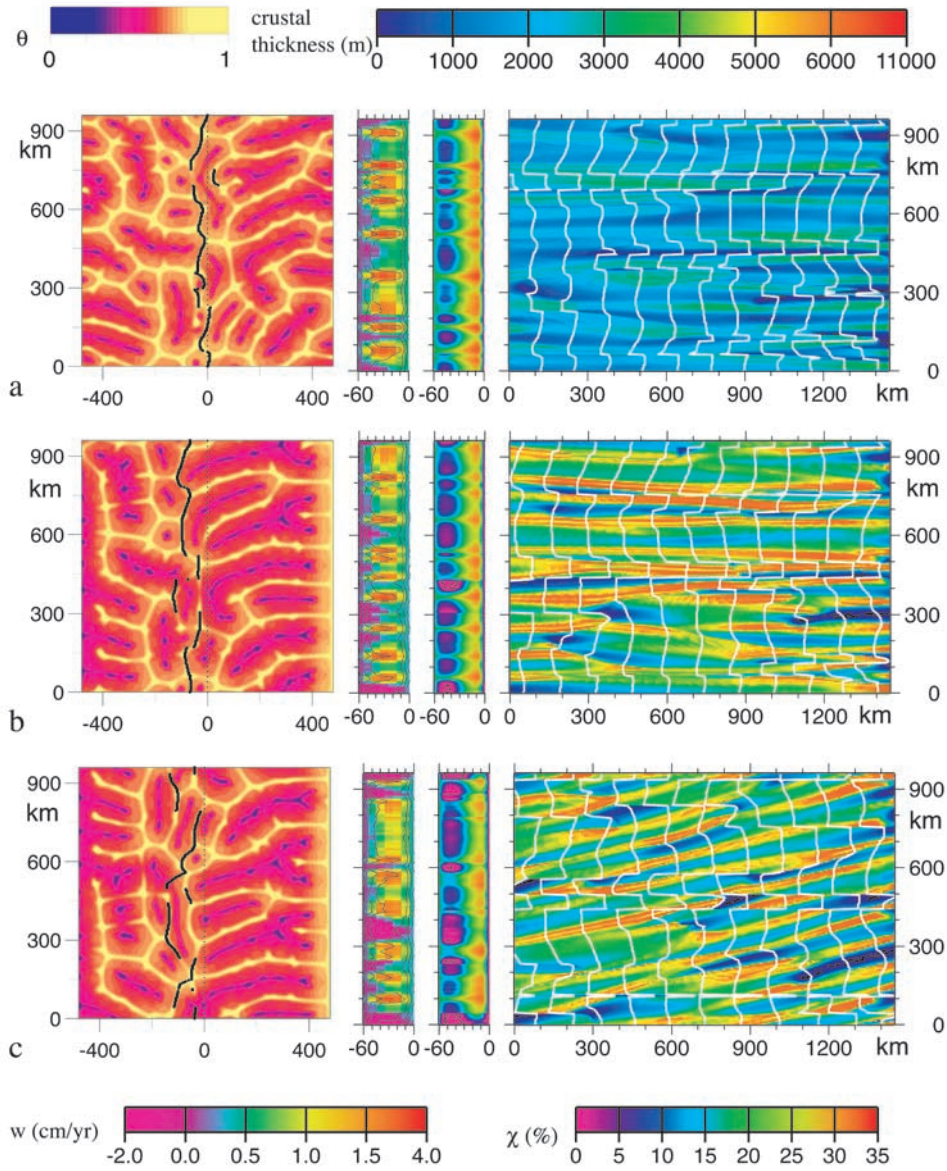

Figure 4. Three distinct experiments with Ra = 30,000. Plotting conventions as in Figure 2. The first experiment (Figure 4a) shows the effect of doubling the spreading velocity: V_{accr} = 34 mm yr^{-1} instead of 17 mm yr^{-1}. In the last two experiments (Figures 4b and 4c) we test the effect of a shear velocity at the bottom of the layer: $\mathbf{V}_{bot}$ = (8 mm yr^{-1}, 0 cm yr^{-1}) and $\mathbf{V}_{bot}$ = (8 mm yr^{-1}, 8 mm yr^{-1}), respectively. The experiments in Figures 4b and 4c last 90 Myr, while the one in Figure 4a lasts 45 Myr. Other parameter values are those of the model drawn in Figures 2c and 3.

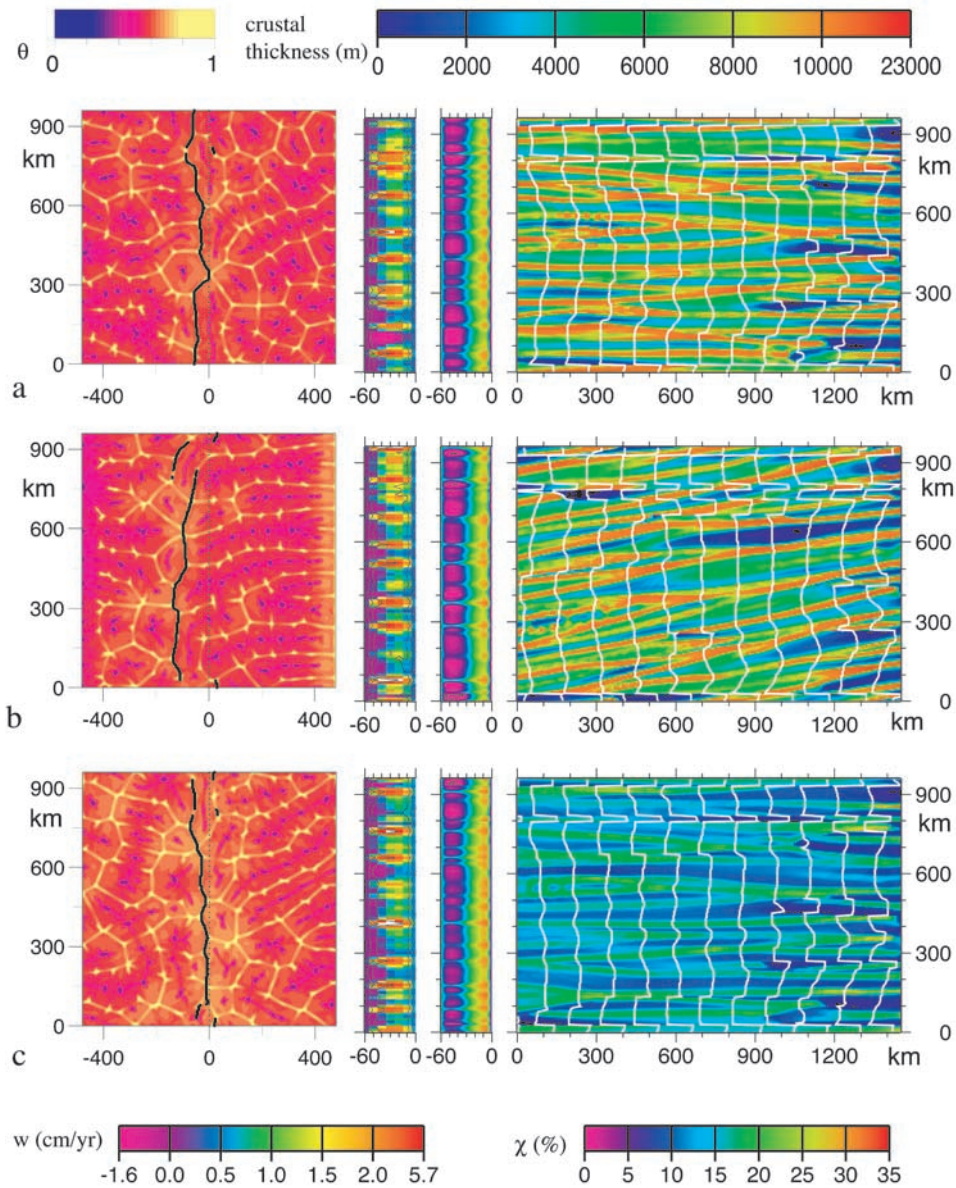

Figure 5. Three distinct experiments with a Ra = 90,000. Plotting conventions are as in Figure 2. The two first experiments (Figures 5a and 5b) are run with a half-spreading velocity V_{accr} = 17 mm yr^{-1}. They differ by the bottom shear velocity which is equal to $\mathbf{V}_{bot}$ = 0 and to $\mathbf{V}_{bot}$ = (8 mm yr^{-1}, 17 mm yr^{-1}) in Figures 5a and 5b, respectively. The experiment in Figure 5c shows the effect of doubling the spreading velocity: V_{accr} = 34 mm yr^{-1} instead of 17 mm yr^{-1} (here also $\mathbf{V}_{bot}$ = 0). The experiments in Figures 5a and 5b last 90 Myr, while the one in Figure 5c lasts 45 Myr.

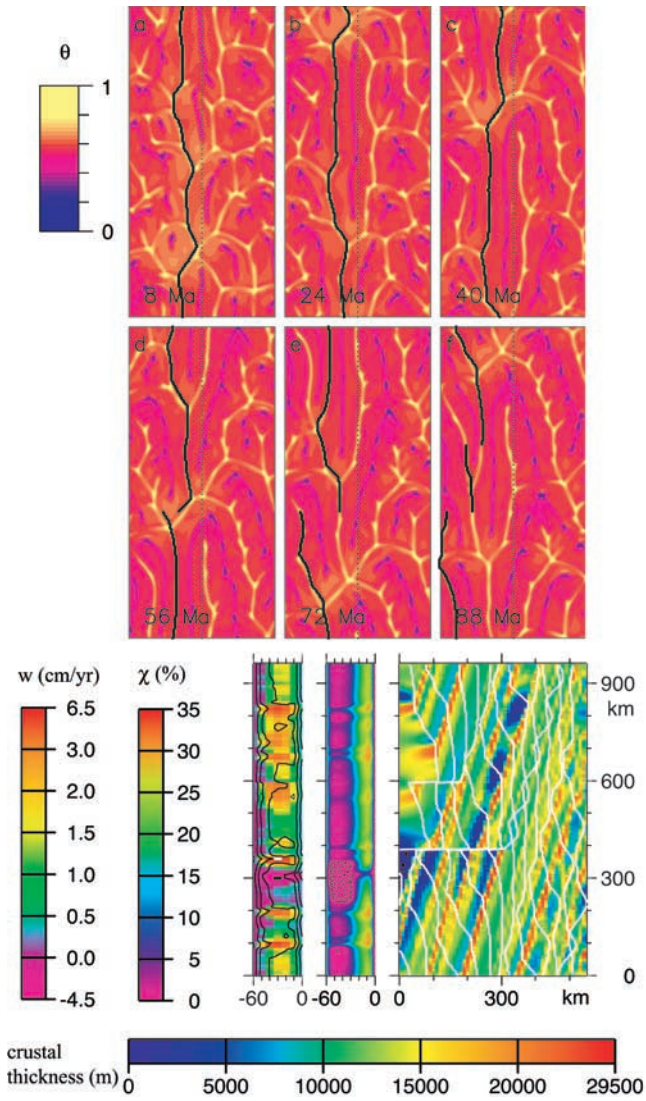

Figure 6. Mantle flow, isochrones, and magmatic lineations when a hot spot located beneath the ridge crest drives a very strong north-south mantle flow. Parameter values are those of the North Atlantic plates next to the Icelandic hot spot. The half-spreading velocity is 8.5 mm yr^{-1}. The Rayleigh number of the experiment Ra = 90,000. The bottom shear velocity $\mathbf{V}_{bot}$ = (0 mm yr^{-1}, 70 mm yr^{-1}). The experiment is initiated with the 90 Ma snapshot of the temperature field of Figure 5a experiment. (bottom left) The ridge plane isolines at the end of the experiment for vertical velocity w, temperature, and the melt fraction by weigh. (bottom right) The 90 Ma maps of the crustal lineations and isochrons. The crustal thickness is 13 km on average. (top) Several snapshots of the middepth temperature in a window restricted to the central part of the computing box. Note the development of major transform faults. Plotting conventions are as in Figure 2.